

UTILIZING OPTOMECHANICS TO ENHANCE MEMS  
OSCILLATORS AND INERTIAL SENSORS

A Thesis

Presented to the Faculty of the Graduate School  
of Cornell University

in Partial Fulfillment of the Requirements for the Degree of  
M.S.

by

Matthew Joseph Storey

January 2015

© 2015 Matthew Joseph Storey

ALL RIGHTS RESERVED

## ABSTRACT

Virtually every communications system today requires some form of reference oscillators. The need for miniaturized, batch manufacturable oscillators as chip scale timing references stems from the need to replace the well-established, high performing, albeit expensive quartz oscillators without compromising on performance. MEMS oscillators have recently found applications in various consumer electronic applications. With numerous advances in fabrication technology and materials processing, these oscillators are being pushed to create a presence in the high performance base-band market and high frequency applications. Scaling MEMS oscillators to high frequencies presents challenges in terms of reduced transduction efficiencies and material limits on quality factors. Opto-mechanical transduction offers higher sensitivity and opens up possibilities to interrogate high frequency mechanical resonances hitherto inaccessible. MEMS has also found a strong foothold in the several markets for inertial sensors. Typical MEMS accelerometers and gyroscopes operate at low frequencies (kHz) through electrostatic drive and sense. A limiting factor in the sensitivity of these sensors is the electronic noise in the sense circuitry.

This thesis investigates how opto-mechanics can benefit the field of MEMS in low-phase noise oscillators and inertial sensors (gyroscopes). Using a previously demonstrated opto-acoustic oscillator (OAO), a driving scheme is presented for an OAO by simultaneously exploiting radiation-pressure (RP) and RF feedback oscillation mechanisms to achieve significantly lower phase noise than could be realized by either phenomenon solely. A theoretical model and experimental results are presented corroborating this scheme, demonstrating a silicon OAO operating

at 175 MHz with a phase noise of -128.6 dBc/Hz at 1 MHz offset with 2.77 dBm RF output power, resulting in a 10dB far-from-carrier phase noise improvement. An opto-mechanical transduction scheme is then presented which is selective to sensing the wine glass modes in an on-chip integrated silicon mechanical resonator. By utilizing two orthogonal waveguides for opto-mechanical sensing at the anti-nodes of the desired wine glass mode, the phase difference between the wine glass modes can be used to selectively sense the desired wine glass modes as compared to other modes. The theoretical model for this transduction scheme is presented followed by the mechanical and optical design of several potential resonators. The design of the resonator, drive electrodes, and tunable waveguides are all explored. These designs are experimentally characterized for the 22.3 MHz and 25 MHz wineglass modes. Optical resonances were shown with loaded optical quality factors as high as 95k. Tunable optical coupling was shown with a DC bias gap-closing waveguide design that reduced the extinction of the optical resonance by 7dB with an applied voltage of -43.9V. Differential electrostatic drive was implemented and showed a 15dB suppression of the unwanted wineglass mode. The RF transmission of the wineglass modes for both waveguides showed out-of-phase signals for the wineglass mode of interest and in-phase signals for the other wineglass mode, consistent with what is needed for balanced differential detection. An application considered for these resonator designs and differential sensing scheme is as a vibratory gyroscope. The resonator designs are modified to reduce the wineglass mode splitting to 50-76kHz. Initial COMSOL simulations were performed by applying external rotations and measuring the displacements at the drive and sense from the resulting coriolis accelerations.

## BIOGRAPHICAL SKETCH

Matthew Joseph Storey was born in Elk Grove Village, IL to Richard and Susanne Storey on January 18<sup>th</sup> 1990. He graduated from James B. Conant high school in 2008. He received a B.S. with honors in Engineering Science from The Pennsylvania State University in 2011 and wrote an honors undergraduate thesis on measuring the defect densities in silicon carbide semiconductor devices. During his undergraduate studies, he was a research assistant at the University of Houston and University of Hawaii-Manoa. He was also a corporate R&D intern at 3M Electronics Lab. He joined the OxideMEMS Lab at Cornell University in November 2012. His work was focused on improving the performance of low phase noise opto-acoustic oscillators and exploring the scalability of these oscillators. He then began to expand this technology to differential opto-mechanical detection with applications in low frequency oscillators and opto-mechanical gyroscopes. In addition to research, he enjoys dancing, ice skating, and is an avid movie watcher.

To my family,  
for their love and encouragement

## ACKNOWLEDGEMENTS

I would like to begin by thanking my advisor, Sunil Bhave, for all of his assistance and guidance throughout my Masters degree. He introduced me to the field of MEMS and helped me look at the bigger picture and overall goals of my research. I would also like to thank Prof. Pollock and Prof. Lipson for being on my qualifying exam committee. My discussions about my research with Prof. Weinstein at MIT were very informative, especially towards the end of my time at Cornell. I would also like to thank all of the teachers at Cornell I took courses from. The courses were rigorous, informative, and gave me a new perspective on course instruction and how to approach learning at a top tier university.

Every member of the OxideMEMS group has had a large influence on not only my approach to research, but life as well. Sid was an excellent mentor and I thank him for taking me under his wing and teaching me about fabricating, testing, and analyzing silicon opto-mechanical resonators. I had many informative discussion with Jon and Ryan and valued their input on a myriad of topics. I had a lot of fun hanging out with Ajay in the office on all those late nights. It was a pleasure working with him on the opto-mechanical gyroscope project. I would like to share my deep gratitude toward Tanay and Sachin for giving me a place to stay for several months during the end of my Masters degree. Our discussions about research and life have changed me as a researcher and a person. I would like to thank all of the staff in Cornell's Nanoscale Science and Technology Facility for helping me with my fabrication process and maintaining the tools. Finally, I would like to thank my family for being supportive of my pursuit of a Masters degree and encouraging me throughout my academic career.

## TABLE OF CONTENTS

Biographical Sketch . . . . .	iii
Dedication . . . . .	iv
Acknowledgements . . . . .	v
Table of Contents . . . . .	vi
List of Tables . . . . .	vii
List of Figures . . . . .	viii
<b>1 Introduction</b>	<b>1</b>
1.1 Micromechanical Resonators and Oscillators . . . . .	1
1.2 Cavity Opto-Mechanics . . . . .	2
<b>2 Radiation-Pressure Enhanced Opto-Acoustic Oscillator</b>	<b>3</b>
2.1 Opto-Acoustic Oscillator (OAO) . . . . .	4
2.1.1 Theoretical Model . . . . .	4
2.1.2 Non-dimensionalized Dynamics . . . . .	6
2.1.3 Phase Noise Improvement . . . . .	7
2.2 Numerical Simulations of Oscillating Mechanisms . . . . .	8
2.3 Experimental Characterization . . . . .	9
<b>3 Opto-Mechanically Sensed Gyroscope (OMG)</b>	<b>15</b>
3.1 Differential Opto-Mechanical Detection Scheme . . . . .	15
3.2 Selective Transduction of Mechanical Wineglass Modes in Silicon . . . . .	22
3.2.1 Design of Mechanical Wineglass Modes . . . . .	22
3.2.2 Electrode Design for Electrostatic Drive . . . . .	25
3.2.3 Optical Coupling Design and Phase Matching . . . . .	28
3.2.4 Electrostatically Tunable Waveguides . . . . .	32
3.2.5 Experimental Characterization . . . . .	36
3.3 Silicon MEMS Wineglass Gyroscope with Differential Optical Coriolis Sensing . . . . .	41
3.3.1 Adjusted Ring Design to Reduce Mode Splitting . . . . .	42
3.3.2 Modeling of Coriolis Force Displacements . . . . .	44
<b>4 Conclusion and Future Work</b>	<b>46</b>
<b>A Fabrication Process for Silicon Opto-Mechanical Resonators</b>	<b>47</b>
A.1 Process Flow for OAO Silicon Resonators . . . . .	47
A.2 Process Flow for OMG Silicon Resonators . . . . .	47
A.2.1 List of Process Steps for Full Run . . . . .	47
A.2.2 List of Process Steps for Short Run . . . . .	58
<b>Bibliography</b>	<b>67</b>

## LIST OF TABLES

2.1	Phase noise comparisons at offset frequencies . . . . .	14
-----	---	----

## LIST OF FIGURES

2.1	Scanning electron micrograph (SEM) of the 2-coupled-ring resonator. The resonator-waveguide gap is 100nm, each ring has an inner radius of $5.7\mu\text{m}$ and outer radius of $9.5\mu\text{m}$ and the resonator-electrode gap is 130nm. . . . .	4
2.2	Limit cycle comparisons of the three driving schemes. For RP enhanced RF feedback, plot (a) is when amplifier gain is held constant and plot (b) is for the total closed loop gain held constant. . . . .	9
2.3	RF Transmission spectrum for the opto-acoustic resonator measured in vacuum ( $30\mu\text{Torr}$ ) and low temperature (80 K). The mechanical mode at 175.3 MHz corresponds to the fundamental radial expansion mode (inset: mode-shape) with a quality factor of 6,000. . . . .	10
2.4	Experimental setup for radiation pressure oscillations. . . . .	11
2.5	Experimental setup for feedback oscillations. . . . .	12
2.6	Phase noise data for all three driving mechanisms. For each plot, the RF output signal power and driving scheme is given. . . . .	12
2.7	Phase noise data normalized to the power consumption. For each plot, the input optical power and driving scheme is given. . . . .	13
3.1	Illustration of the sensing mechanisms for differentiating gap change and path length change modulation from the optomechanical resonator. . . . .	16
3.2	Wineglass mode ring resonator designs. Images (a-c) show the first generation resonator design and its non-degenerate wineglass mode shapes and corresponding frequencies. Images (d-f) show the second generation ring design and corresponding mode shapes. . . . .	23
3.3	SEM of the first generation resonator with direct differential electrostatic drive (a). The ring has an outer radius of $18\mu\text{m}$ , inner radius of $12\mu\text{m}$ , and base radius of $4\mu\text{m}$ . The resonator-waveguide gap is 80nm and resonator-electrode gap is 100nm. The optical waveguide tuning capacitor gap is 150nm. Wineglass mode shapes of first generation devices are shown in (b) with same frequencies as Figure 3.2 (b-c). . . . .	25
3.4	SEM of the second generation resonator with attached differential electrostatic drive (a). The ring has an outer radius of $15\mu\text{m}$ , inner radius of $11.3\mu\text{m}$ , and base radius of $2.3\mu\text{m}$ . The resonator-waveguide gap is 90nm and resonator-electrode gap is 100nm. The optical waveguide tuning capacitor gap is 100nm. Wineglass mode shapes of modified second generation devices are shown in (b) with resonant frequencies of 20.99 MHz (top) and 21.91 MHz (bottom). . . . .	26

3.5	SEM of the second generation resonator with 2-coupled-ring differential electrostatic drive (a). The ring has an outer radius of $15\mu\text{m}$ , inner radius of $11.3\mu\text{m}$ , and base radius of $2.3\mu\text{m}$ . The coupling beams are a modified $\lambda/2$ design with a length of $47\mu\text{m}$ . The resonator-waveguide gap is $90\text{nm}$ and resonator-electrode gap is $100\text{nm}$ . The optical waveguide tuning capacitor gap is $100\text{nm}$ . Wineglass mode shapes of modified second generation devices are shown in (b) with resonant frequencies of $20.68\text{ MHz}$ (top) and $22.70\text{ MHz}$ (bottom). . . . .	27
3.6	Plot (a) shows the effective index of the waveguide mode (translated to the disk edge) as a function of waveguide width assuming a gap of $90\text{ nm}$ . The effective index of several TE radial modes for first generation devices are marked as points on the curve, corresponding to waveguide widths for achieving phase matching at $1550\text{ nm}$ . First generation devices were phased matched to the 8th radial order TE mode with the $ E_r ^2$ profile given in (b). . . . .	29
3.7	Plot (a) shows the effective index of the waveguide mode (translated to the disk edge) as a function of waveguide width assuming a gap of $90\text{ nm}$ . The effective index of several TE radial modes for second generation devices are marked as points on the curve, corresponding to waveguide widths for achieving phase matching at $1550\text{ nm}$ . Second generation devices were phased matched to the 3rd and 4th radial order TE modes with the $ E_r ^2$ profiles given in (b). . . . .	31
3.8	The deformation profile along the waveguide for all three waveguide tuning designs are compared in the graph above. The shaded graph region is the approximate coherent coupling length of a point coupled waveguide to a traveling wave resonator (TWR). The shapes of the statically displaced waveguides are shown in (A) for the first generation, and (B-C) for the second generation. . . . .	33
3.9	Graph of the DC voltage applied across the tunable waveguide vs. waveguide gap change at the coupling point. Pull-in of the tuning element limits the maximum tuning range and voltage that can be applied (marked as dashed lines). Negative tuning (neg) refers to moving the waveguide away from the resonator and positive tuning (pos) moves the waveguide toward the resonator. . . . .	34
3.10	Schematic of the differential drive and sense experimental setup. . .	36
3.11	Plot (a) shows an optical resonance measured on the first generation devices with a loaded optical Q of $95\text{k}$ . Plot (b) shows the tuning of the coupling to another optical resonance of the resonator by changing the resonator-waveguide gap using a gap change capacitor (first generation device and waveguide tuning). . . . .	37

3.12	For a first generation device, the amplitude of the n=2 wineglass modes for single-ended (black) and differential (blue) electrostatic drive measured using optical waveguide on port 2. The electrodes are designed to favorably drive the 45°-135°(22.3Mhz) mode. Measurements were carried out with input optical power of 11.5dBm at 1528nm, input RF power of -5dBm (-2dBm) for single-ended (differential) drive with a DC bias of 12V. . . . .	38
3.13	For the same first generation device, plots show the amplitude (above) and phase (below) of the single-end driven 45°-135° (a) and 0°-90° (b) n=2 wineglass modes measured by the two optical waveguides on port 2 (red) and port 3 (green). The optical waveguides are positioned at the anti-nodes (nodes) of the 45°-135° (0°-90°) mode and hence at the respective resonances show a 180° (0°) difference in the signal phase. Inset shows COMSOL simulations of the respective modes. Measurements were done with input optical power of 11.5 dBm at 1528nm, input RF power of -5dBm and a DC bias of 12V. . . . .	40
3.14	Second generation wineglass resonator designs had additional spokes added with unequal circle springs to reduce the mode splitting from the anisotropic nature of single crystal Silicon. For an attached electrode driving scheme (a-c), the circle springs had radii of 1.8μm and 2μm. From COMSOL simulations, The frequency split was reduced to 54kHz. For a 2-coupled-ring electrode driving scheme (d-f), the circle springs had radii of 1.75μm and 2.12μm. From COMSOL simulations, The frequency split was reduced to 76kHz. For initial COMSOL simulations to model the effect of coriolis force, the "drive" wineglass mode was actuated (blue lines) and the displacement of the "sense" wineglass mode was examined (red dot). . . . .	43
3.15	For the attached electrode driving scheme, plot (a) shows the displacement of the driven wineglass mode at one of its anti-nodal points. The displacement at the sense wineglass mode's anti-nodal point (b) is compared with and without rotation present (coriolis force). . . . .	44
3.16	For the 2-coupled-ring electrode driving scheme, plot (a) shows the displacement of the driven wineglass mode at one of its anti-nodal points. The displacement at the sense wineglass mode's anti-nodal point (b) is compared with and without rotation present (coriolis force). . . . .	45

# CHAPTER 1

## INTRODUCTION

### 1.1 Micromechanical Resonators and Oscillators

MEMS technology has enabled a class of mechanical oscillators with very small size, low cost, and potential for CMOS integration [1, 2, 3]. These MEMS-based oscillators have better noise performance and frequency stability compared to conventional electrical oscillators, due to the high quality factor of the mechanical resonance. This has the potential to bridge the gap between high-performance, non-CMOS oscillator technology and low-performance CMOS compatible oscillators. For current oscillator technologies, replacing quartz resonators with MEMS resonators integrated with CMOS on a single chip would reduce the form factor, system complexity, and cost [4].

Several timing and frequency control functions have been realized with MEMS technology, which have competing power consumption with additional benefits from scaling down to microns [3, 5]. One outcome from scaling is vibrating RF MEMS devices now being able to reach frequencies needed for RF functions in wireless applications. Scaling these MEMS resonators to higher frequencies (5-10GHz) presents several challenges. For oscillators, the motional impedance of the electrostatically transduced resonators is large, making it difficult to close the loop on the oscillator. Current research efforts include developing new transduction schemes with reduced motional impedance at GHz frequencies [6]. Resonant body transistors, which integrate a sense transistor into the body of the resonator, have been demonstrated with center frequencies of 11.7GHz [7] and 39GHz [8]. These resonators, however, are not easily incorporated into oscillators in part to their large

parasitics that hinder the sense signal. Previously, our group has demonstrated an opto-mechanically transduced MEMS oscillator designed in silicon nitride with zero flicker noise [9], which greatly simplifies the oscillator design and does away with active noise sources that would otherwise add flicker noise, thereby degrading the oscillator phase noise. While this device was at lower frequencies, using the same opto-mechanical transduction scheme for sensing, 2GHz opto-acoustic oscillators have also been demonstrated in silicon [10].

## 1.2 Cavity Opto-Mechanics

In the MEMS community, light having the ability to sense displacement (nanometer scale) has been shown with stroboscopic interferometry [11], homodyne Michelson interferometry [12] and heterodyne laser-Doppler interferometry [13]. The dynamics of light exciting a mechanical resonant mode through radiation pressure force was first demonstrated in ultra high quality factor silica micro toroids [14, 15]. This brought the fields of optical micro resonators and mechanical resonators together, forming the field of cavity optomechanics. Progress has been made in this field in terms of displacement sensitivity at high frequencies and further investigation into this displacement sensing scheme will be carried out in the following chapters.

CHAPTER 2  
**RADIATION-PRESSURE ENHANCED OPTO-ACOUSTIC  
OSCILLATOR**

Opto-mechanical resonator based oscillators have been previously demonstrated in both open and closed loop configurations utilizing radiation pressure (RP) [9, 16] and RF feedback (RF) [17], respectively. Simultaneous incorporation of these oscillating mechanisms can be achieved with a 2-coupled-ring opto-mechanical resonator. Figure 2.1 shows an SEM of our device. The coupled resonator can be transduced through either capacitive electrostatics or evanescent optical coupling. While each ring utilizes a different forcing mechanism, the displacement is conserved and transferred between ring resonators through the  $\lambda/2$  coupling beam. In the following sections, a model is presented for the 2-coupled-ring opto-mechanical cavity dynamics utilizing both RP and RF feedback forces. This model was nondimensionalized to examine the relative affects between these driving mechanisms and simulations were performed. The 2-coupled-ring resonator was fabricated and tested in vacuum at low temperatures under three operating conditions - RP, RF feedback, and both simultaneously. The phase noise of the oscillator was measured in all three cases and compared at both close-to-carrier and far-from-carrier offset frequencies.

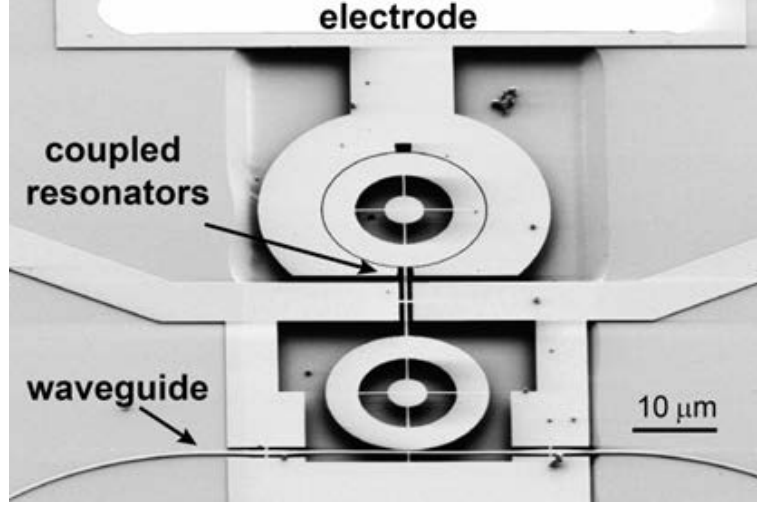


Figure 2.1: Scanning electron micrograph (SEM) of the 2-coupled-ring resonator. The resonator-waveguide gap is 100nm, each ring has an inner radius of  $5.7\mu\text{m}$  and outer radius of  $9.5\mu\text{m}$  and the resonator-electrode gap is 130nm.

## 2.1 Opto-Acoustic Oscillator (OAO)

### 2.1.1 Theoretical Model

The dynamics of an opto-mechanical cavity have been extensively studied in previous work [18]. The displacement  $u$  and optical field  $\sqrt{\hbar\Omega_L}a$  inside the cavity are related through the following coupled equations of motion [19]

$$m\ddot{u} + m\gamma_0\dot{u} + m\Omega_0^2u = F_{rp} + F_{rf} \quad (2.1)$$

$$\dot{a} = i(\Delta_0 + g_{om}u)a - \frac{1}{2}\kappa a + \frac{1}{2}\kappa n_{max}^{\frac{1}{2}} \quad (2.2)$$

Here,  $\Omega_0$  is the mechanical resonance frequency,  $m$  is the effective mass, and  $\gamma_0$  is natural damping of the harmonic resonator. The total optical cavity detuning  $\Delta = \Delta_0 + g_{om}u$  is a function of both the laser detuning at zero displacement

$\Delta_0$ , the dynamic displacement of the cavity  $u$ , and the optomechanical coupling coefficient  $g_{om}$ . The total (loaded) optical linewidth  $\kappa = \kappa_i + \kappa_{ex}$  can be expressed as a sum of the intrinsic and extrinsic (coupling) linewidths, respectively. The normalized intra cavity photon number can be expressed as  $n = |a|^2$  and the input power  $P_{in}$  can be expressed in terms of the maximum intra cavity photon number  $n_{max} = 4P_{in}\kappa_{ex}/\kappa^2\hbar\Omega_L$  [19].

The 2-coupled-ring design of our opto-mechanical resonator allows for a unique transduction scheme via simultaneous forcing through both radiation pressure and capacitive electrostatic forces. The force on the cavity generated through radiation pressure is only dependent on the opto-mechanical coupling coefficient and the intra cavity photon number  $F_{rp} = \hbar g_{om}n$  [19].

The RF electrostatic force, however, depends on the feedback loop design incorporating the resonator. In our setup, the cavity's output optical power is sent to a photodetector and converted into a photocurrent. The optical field transmitted from the cavity can be expressed in terms of the input optical field and intra cavity field  $a_{out} = a_{in} - \sqrt{\kappa_{ex}}a$  where  $|a_{out}|^2$  is normalized to the output power and  $|a_{in}|^2$  is normalized to the input power ( $P_{in}$ ) [20]. The total photocurrent is proportional to the output power

$$i_{tot} = |a_{out}|^2 = |a_{in}|^2 + \kappa_{ex}n - 2 \operatorname{Re} \{a_{in}^* a \sqrt{\kappa_{ex}}\} \quad (2.3)$$

Since the input power is constant, the current fluctuations are contained in the difference between the output and input power. Therefore, the photocurrent that is fed back to the resonator can be expressed as  $i_{rf} = |a_{out}|^2 - |a_{in}|^2$ . The photocurrent is then amplified (gain  $G$ ) with appropriate phase shift and electrostatically applied

to the optomechanical resonator to close the feedback loop. The general forcing function for the RF feedback is given as  $F_{rf} = Gi_{rf}$  [21].

### 2.1.2 Non-dimensionalized Dynamics

To better understand the relative interaction between these two forcing mechanisms, the coupled equations of motion are put into a dimensionless form [19]

$$\tilde{u}'' + \tilde{\gamma}_0 \tilde{u}' + \tilde{u} = c_{om} \tilde{n} + c_{om} \tilde{G} \left( \tilde{\kappa}_{ex} \tilde{n} - 2\sqrt{\tilde{\kappa}_{ex}} Re \{ \tilde{a} \} \right) \quad (2.4)$$

$$\tilde{a}' = i \left( \tilde{\Delta}_0 + \tilde{u} \right) \tilde{a} - \frac{1}{2} \tilde{\kappa} \tilde{a} + \frac{1}{2} \tilde{\kappa} \quad (2.5)$$

Here, the time was scaled by the mechanical resonance frequency  $\tau = \Omega_0 t$  and the displacement was scaled as  $\tilde{u} = u g_{om} / \Omega_0$ . All other frequencies were scaled by  $\Omega_0$  [19] such that  $\tilde{\gamma}_0 = \gamma_0 / \Omega_0$ ,  $\tilde{\kappa} = \kappa / \Omega_0$ , and  $\tilde{\Delta}_0 = \Delta_0 / \Omega_0$ . The normalized extrinsic linewidth is a fraction of the total normalized linewidth, which depends on the coupling. In general,  $\tilde{\kappa}_{ex} = \mu \tilde{\kappa}$  where  $0 < \mu < 1$ , but for the rest of this analysis the device is assumed to be critically coupled such that  $\mu = 0.5$ .

The intra cavity optical field was normalized by the maximum photon number such that  $\tilde{a} = a / \sqrt{n_{max}}$  and  $\tilde{n} = n / n_{max}$ . The strength of the radiation pressure force was scaled as  $c_{om} = 2 n_{max} u_{zpm}^2 g_{om}^2 / \Omega_0^2$  and a detailed explanation of the radiation pressure coupling strength can be found in [19]. The strength of the RF feedback force is both a combination of the input optical power contained in  $c_{om}$  and the scaled gain  $\tilde{G}$  from the amplifier. Therefore, the total dimensionless strength of the closed loop RF feedback force is given by  $c_{om} \tilde{G}$ .

### 2.1.3 Phase Noise Improvement

Assuming the harmonic oscillations of the optomechanical cavity have an energy that is proportional to the square of the displacement, the oscillation linewidth can be expressed as [22]

$$\delta\nu = \Delta\nu \left( \frac{k_B T}{m_{eff} \Omega_0^2} \right) \frac{1}{u^2} \quad (2.6)$$

Here,  $\delta\nu$  is the narrowed linewidth,  $\Delta\nu$  is the natural linewidth of the resonator, and  $m_{eff}$  is the effective mass. The relationship between the oscillators linewidth and its phase noise  $\mathcal{L}$  (dBc/Hz) at a carrier offset frequency  $\Delta f$  in the  $1/f^2$  regime is given by [22]

$$\delta\nu = 2\pi \Delta f^2 10^{\mathcal{L}/10} \quad (2.7)$$

By only varying the driving schemes of an OAO, a change in the displacement can vary the degree in which the linewidth narrows. This in turn can change the phase noise at a given carrier offset. Equations 2.6 and 2.7 were combined and the phase noise difference at a constant offset was solved for as a function of the displacement ratio

$$\Delta\mathcal{L} = \mathcal{L}_2 - \mathcal{L}_1 = 20 \log_{10} \left( \frac{u_1}{u_2} \right) \quad (2.8)$$

Equation 2.8 shows that the phase noise improvement is proportional to the ratio of oscillation energies. Therefore, if the displacement of second driving scheme is larger than the first driving scheme ( $u_2 > u_1$ ), then there will be an improvement

in the phase noise ( $\Delta\mathcal{L} < 0$ ).

## 2.2 Numerical Simulations of Oscillating Mechanisms

The relative displacements of the different driving schemes were compared by numerically integrating equations 2.4 and 2.5 for different cases of  $c_{om}$  and  $\tilde{G}$ . Our OAO operates in the unresolved sideband regime (USR) and typically exhibit mechanical quality factors on the order of a couple thousand, so the dimensionless parameters chosen were  $\tilde{\gamma}_0 = 0.0005$ ,  $\tilde{\kappa} = 10$ , and  $\tilde{\Delta}_0 = 3$  [19].

The values for  $c_{om}$  and  $\tilde{G}$  for the three cases are determined from the threshold behavior of both the RF feedback and radiation pressure induced oscillations. The threshold for radiation pressure oscillations was found to be  $c_{om} = 0.015$  and the threshold for closed loop RF feedback was  $c_{om}\tilde{G} = 0.007$ .

The first case is just RP oscillations, so the amplifier gain was set to  $\tilde{G} = 0$  and the radiation pressure coupling coefficient was set to twice the threshold at  $c_{om} = 0.03$ . The second case is for just RF feedback, so the radiation pressure force is set well below threshold at  $c_{om} = 0.005$  and the amplifier gain was set to just above RF feedback threshold at  $\tilde{G} = 2$ . In the third case, both forces were placed above threshold. Since the RF feedback force is a function of both gain terms, two comparisons arise for RP enhanced RF feedback oscillations. As  $c_{om}$  is raised above threshold (0.03), either the amplifier gain  $\tilde{G}$  can be held constant at 2 or the total closed loop gain can be held constant at  $c_{om}\tilde{G} = 0.01$ , which requires reducing the amplifier gain to  $\tilde{G} = 1/3$ .

Figure 2.2 shows the simulation results of the three cases. When the driving

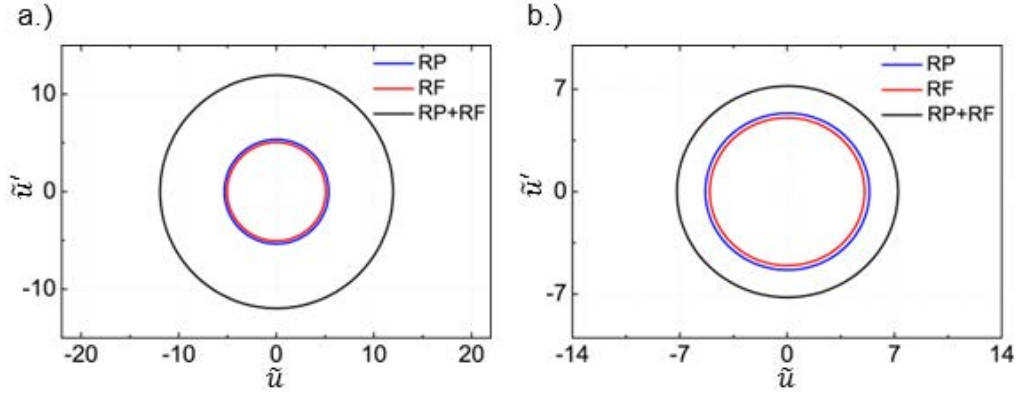


Figure 2.2: Limit cycle comparisons of the three driving schemes. For RP enhanced RF feedback, plot (a) is when amplifier gain is held constant and plot (b) is for the total closed loop gain held constant.

scheme was only radiation pressure or RF feedback, the oscillator reached a steady limit cycle with scaled displacement amplitude of approximately 5. When both driving schemes were incorporated while holding the amplifier gain constant, the scaled amplitude reached a value of 12 (plot (a) of figure 2.2). If the total closed loop gain was held constant, the scaled amplitude reached a value of 7.2 (plot (b) of figure 2.2). Plugging these values into equation 2.8, the resulting phase noise improvement would be approximately 8 dB and 3 dB, respectively.

### 2.3 Experimental Characterization

The 2-coupled-ring opto-mechanical resonator was fabricated on a silicon-on-insulator (SOI) wafer and the fabrication process was described in detail in [17]. All experiments were performed in a Lakeshore probe station under vacuum (30Torr) using Liquid Nitrogen to cool the chamber to 80 K. An optical probe was used to send continuous wave (CW) light into the device through a pair of on-chip grating

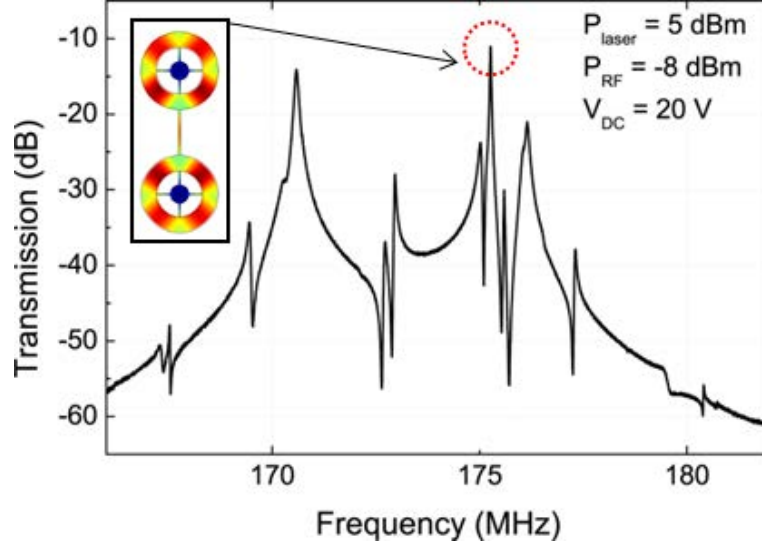


Figure 2.3: RF Transmission spectrum for the opto-acoustic resonator measured in vacuum ( $30\mu\text{Torr}$ ) and low temperature (80 K). The mechanical mode at 175.3 MHz corresponds to the fundamental radial expansion mode (inset: mode-shape) with a quality factor of 6,000.

couplers. A GSG probe was used to apply an RF signal to the bond pads, which connected to the electrodes around the resonator.

Open loop measurements were performed on the optoacoustic resonator to determine the RF transmission spectrum of the mechanical mode of interest. As the applied RF signal was swept, the transmitted power was sent to a photodetector and the resulting photocurrent was input to a Network Analyzer. Figure 2.3 shows the electromechanical transmission measurement for the fundamental radial mode. The resonance frequency (175.3 MHz) and mechanical quality factor (6,000) were estimated through a Lorentzian curve fit.

For comparison purposes, the phase noise performance of the opto-mechanical resonator based oscillator was first evaluated for RP and RF feedback separately. Since the RP and RF feedback driving mechanisms differ in their application to

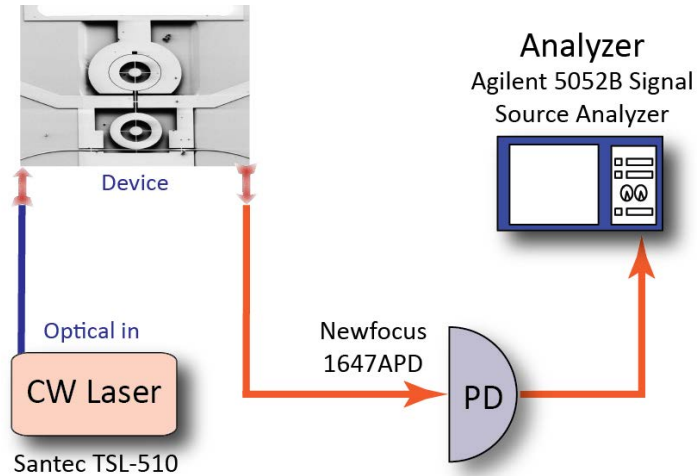


Figure 2.4: Experimental setup for radiation pressure oscillations.

the resonator, this experiment required two separate setups. Figure 2.4 shows the setup for a RP driven opto-mechanical oscillator. A CW diode laser was input to the device and then the output optical power is measured with a Newfocus 1647 photodetector and sent to the phase noise analyzer. RP induced oscillations are achieved by blue detuning the laser within the optical resonance and using an input power above threshold [9, 16].

To ensure that the only means of achieving oscillations is by closing the feedback loop, the laser power is reduced below the threshold for RP oscillations. To create a RF feedback oscillator, the output RF signal from the photodetector is amplified and the required phase shift is introduced to overcome the FB oscillation threshold. The signal is sent through a 3dB splitter and one half is applied to the resonator through the GSG probe while the other half is sent to the phase noise analyzer. Figure 2.5 shows the experimental setup for the RF feedback oscillator. To achieve oscillations induced simultaneously by both RP and RF feedback, the closed loop setup shown in Figure 2.5 is used with the laser blue detuned and with the optical power raised above RP threshold conditions.

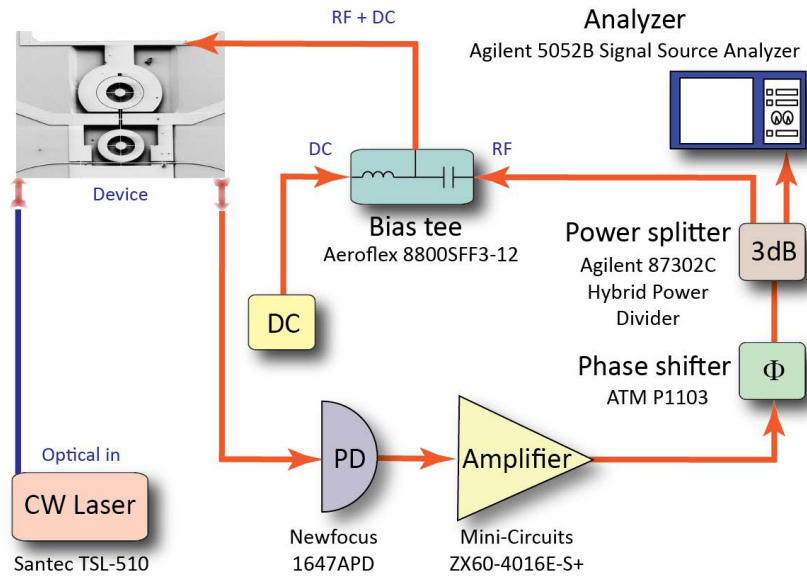


Figure 2.5: Experimental setup for feedback oscillations.

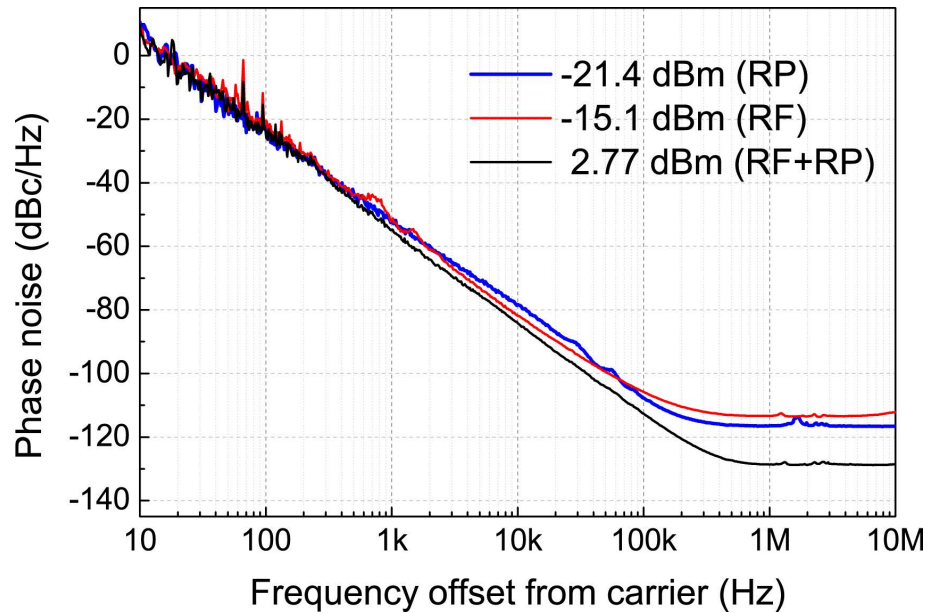


Figure 2.6: Phase noise data for all three driving mechanisms. For each plot, the RF output signal power and driving scheme is given.

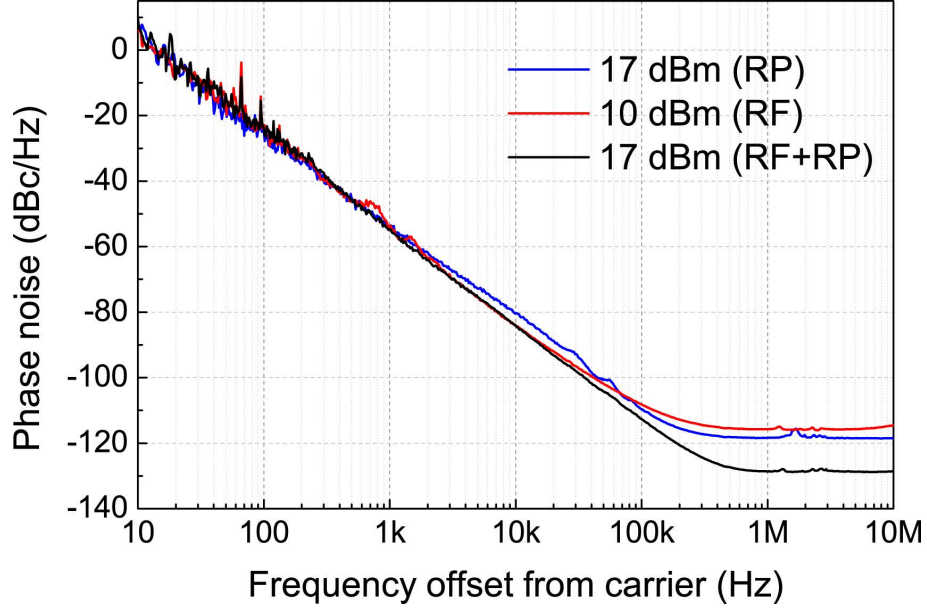


Figure 2.7: Phase noise data normalized to the power consumption. For each plot, the input optical power and driving scheme is given.

Using the setup in figure 2.4, the device was driven into RP oscillations at an input optical power of 17 dBm with a determined RP threshold of 11 dBm. The setup in figure 2.5 was then used to obtain RF feedback oscillations with an input optical power below RP threshold (10 dBm). While in the same closed loop configuration, the input optical power was increased well above threshold (17 dBm) to observe RP enhanced RF feedback oscillations. Any further increase in laser power would result in thermal nonlinearities and chaotic oscillations. All of the closed loop measurements were carried out with 30 V DC bias. Figure 2.6 shows the resulting phase noise for the three measurements, along with the carrier powers and driving scheme. The individual RP and RF feedback oscillations had the lowest carrier powers (-21.4 dBm and -15.1 dBm, respectively) with comparable phase noise performance. The simultaneous RP and RF feedback oscillations demonstrated a large increase in carrier power (2.77 dBm) while experiencing an improvement in the far-from-carrier phase noise.

Table 2.1: Phase noise comparisons at offset frequencies

Operation mode	(Normalized power consumption)		
	Phase Noise (dBc/Hz)		
	1 kHz Offset	100 kHz Offset	1 MHz Offset
RP	-53.62	-109.6	-118.4
RF	-53.95	-108.2	-115.8
RP + RF	-54.74	-112.6	<b>-128.6</b>

The phase noise measurements were normalized to the oscillators laser and amplifier power consumption and compared in figure 2.7 and table 2.1 (photodetector power consumption was too large and would have diminished the normalizations effectiveness). The RP enhanced RF feedback oscillations had no  $1/f^4$  or higher order noise and the close-to-carrier phase noise is dominated by  $1/f^3$  flicker noise from both the amplifier and input laser. A 10dB improvement in far-from-carrier phase noise was observed.

The 2-coupled-ring resonator based oscillator with a mechanical quality factor of 6,000 and resonant frequency of 175.3 MHz was tested under vacuum (30Torr) and low temperature (80 K) for different driving schemes. Simultaneous RP and RF feedback induced oscillations resulted in an increased RF output signal power (2.77 dBm) when compared to only RP (-21.4 dBm) and RF feedback (- 15.1 dBm) oscillations. The combined driving scheme resulted in more energy stored in the oscillator and a 10dB improvement in far-from-carrier phase noise (1MHz).

## CHAPTER 3

### OPTO-MECHANICALLY SENSED GYROSCOPE (OMG)

The silicon resonator presented in this work is made on a silicon-on-insulator (SOI) platform. The resonator can be driven electrostatically either through a single electrode, which doesn't favor any mode, or through two differential electrodes that favor the intended wine glass mode. Mechanical motion is sensed through the modulation of light in the waveguides, which has been shown to be sensitive. Modulation can result from path-length changes from the resonator expanding and contracting, or from optical coupling changes as a result of the resonator changing the gap between the waveguide. In order to increase the selectivity for the desired wine glass mode, the signals from the waveguides must be balanced to perform differential optical detection. Due to fabrication errors, the waveguide-resonator gap will not be equal and therefore optical performance tuning is needed. This work implements waveguide tuning to correct the coupling mismatch. Initial experimental characterization has been shown for this differential optical detection scheme. The last section of this chapter looks at the potential application of this detection scheme in an electrostatically driven opto-mechanically sensed gyroscope (OMG), including any necessary modifications to the mechanical resonator design.

#### 3.1 Differential Opto-Mechanical Detection Scheme

Opto-mechanical resonators have been shown to have high displacement sensitivity [23], but typical displacement sensing schemes based on the intensity modulation of incident light [24] aren't selective to any specific mechanical mode. These detection schemes focus on the dispersive coupling coefficient  $g_{om}$  [25]. This opto-mechanical coupling coefficient is in general largest for the fundamental mechanical mode,

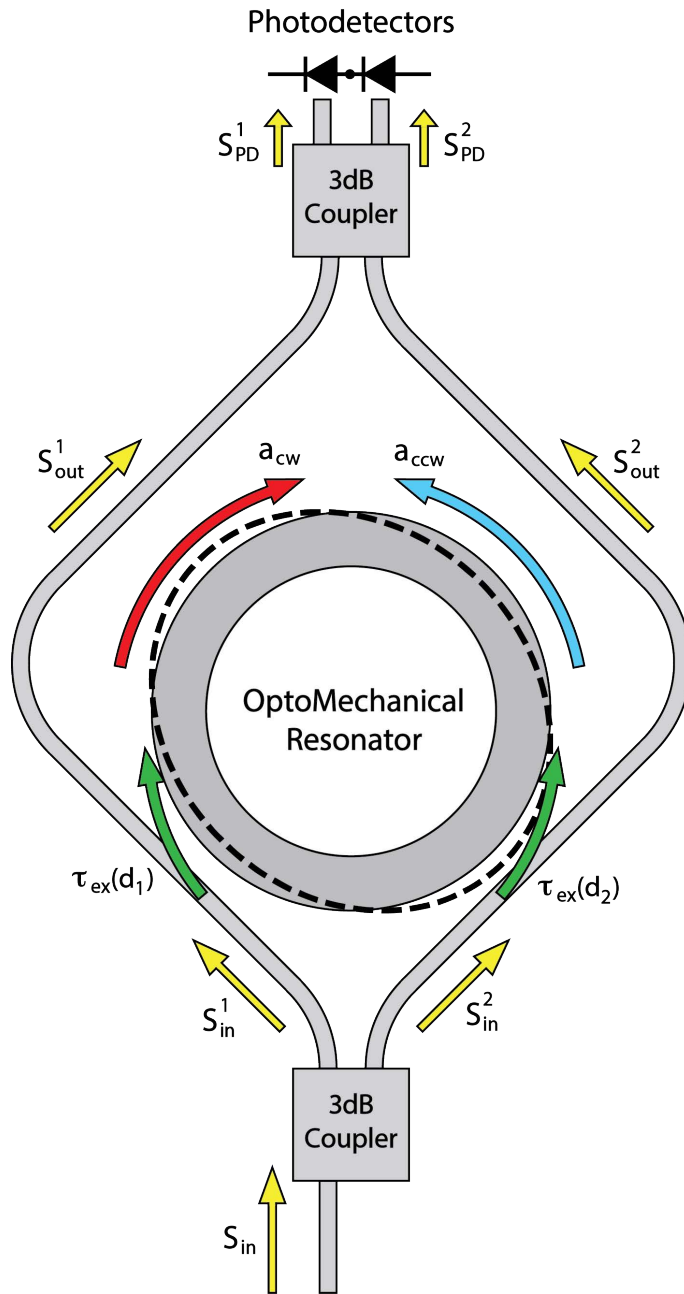


Figure 3.1: Illustration of the sensing mechanisms for differentiating gap change and path length change modulation from the optomechanical resonator.

resulting in that mode having the largest detected signal. For example, in annular ring and disk geometries, the largest  $g_{om}$  and signal level is for the fundamental radial breathing mode.

Another opto-mechanical transduction mechanism to consider is the reactive coupling coefficient [25]. While the dispersive coupling coefficient is represented as the shift in optical cavity resonance per mechanical displacement, the reactive coupling coefficient can be described as the change in the resonator-waveguide coupling per mechanical displacement [25].

A new opto-mechanical detection scheme is presented to distinguish the signal levels resulting from both coupling coefficients. A schematic of the detection scheme is shown in Figure 3.1. Input light  $s_{in}$  is first sent through a 3dB coupler to split the light equally into two waveguides, as  $s_{in}^1$  and  $s_{in}^2$ . After interacting with the mechanical resonator and intracavity light  $a_{cw}$  and  $a_{ccw}$ , the output light  $s_{out}^1$  and  $s_{out}^2$  are again sent through a 3dB coupler where the resulting light  $s_{PD}^1$  and  $s_{PD}^2$  are input to a balanced photodetector setup, resulting in a differential and common signal. Here, all the intracavity light  $|a_k|^2$  is normalized to energy while the light traveling through the waveguides  $|s_k^k|^2$  is normalized to power.

For the first 3dB coupler, the phase and amplitude relations between the input laser field  $s_{in}$  and the two input light fields to the orthogonal waveguides are shown in equation 3.1.

$$\begin{bmatrix} s_{in}^1 \\ s_{in}^2 \end{bmatrix} = \frac{1}{\sqrt{2}} \begin{bmatrix} 1 & i \\ i & 1 \end{bmatrix} \begin{bmatrix} s_{in} \\ 0 \end{bmatrix} \quad (3.1)$$

Once the input power is split between the waveguides, the light's interaction

with the resonator is described by the equations of motion for the intracavity fields  $a_{cw}$  and  $a_{ccw}$  in equations 3.2 and 3.3 [19, 26].

$$\frac{da_{cw}}{dt} = -i\Delta(x) a_{cw} - \frac{1}{2\tau} a_{cw} + i\mu a_{ccw} + i \frac{s_{in}^1}{\sqrt{\tau_{ex}(d_1)}} \quad (3.2)$$

$$\frac{da_{ccw}}{dt} = -i\Delta(x) a_{ccw} - \frac{1}{2\tau} a_{ccw} + i\mu a_{cw} + i \frac{s_{in}^2}{\sqrt{\tau_{ex}(d_2)}} \quad (3.3)$$

Here,  $a_{cw}$  is the field amplitude of the clockwise-propagating cavity field and  $a_{ccw}$  is the counter clockwise-propagating field amplitude. The detuning of the optical cavity resonance can be approximated to the first order as  $\Delta(x) = \Delta + g_{om}x$ , where  $g_{om} = -\frac{\partial\omega_0}{\partial x}$  is the dispersive coupling coefficient,  $x$  is the displacement of the mechanical resonator, and the cavity detuning at  $x = 0$  is a function of the input laser frequency  $\omega_L$  and optical cavity resonance  $\omega_0$  ( $\Delta = \omega_L - \omega_0$ ). The total decay time of the intracavity light is given as  $\frac{1}{2\tau} = \frac{1}{2\tau_0} + \frac{1}{2\tau_{ex}(d_1)} + \frac{1}{2\tau_{ex}(d_2)}$  where  $\tau_0$  is the intrinsic decay time of the resonance, and  $\tau_{ex}(d_1)$  and  $\tau_{ex}(d_2)$  are the coupling rates at the two coupling points with gaps of  $d_1$  and  $d_2$ , respectively. The cross coupling coefficient  $\mu$  between the intracavity modes is a result of back scattering from cavity surface roughness.

The transmitted light through each waveguide can be expressed as a function of both the input light and intracavity fields in equations 3.4 and 3.5.

$$s_{out}^1 = s_{in}^1 - \frac{a_{cw}}{\sqrt{\tau_{ex}(d_1)}} \quad (3.4)$$

$$s_{out}^2 = s_{in}^2 - \frac{a_{ccw}}{\sqrt{\tau_{ex}(d_2)}} \quad (3.5)$$

The following analysis assumes non-degenerate mechanical modes where for the mode of interest the waveguides are placed orthogonally at the mechanical anti-

nodes (example wineglass mode is shown as dashed line in figure 3.1). Here, the waveguide-resonator gaps as a function of the mechanical displacement are defined as  $d_1 = d_0 + x$  and  $d_2 = d_0 - x$ .

Since the coupling gaps are a function of the mechanical displacement, the coupling rates can be approximated to first order as a function of displacement, given as

$$\frac{1}{\tau_{ex}(d_1)} = \frac{1}{\tau_{ex}(d_0)} - \frac{x}{(\tau_{ex}(d_0))^2} \frac{\partial \tau_{ex}(d_0)}{\partial x} \quad (3.6)$$

$$\frac{1}{\tau_{ex}(d_2)} = \frac{1}{\tau_{ex}(d_0)} + \frac{x}{(\tau_{ex}(d_0))^2} \frac{\partial \tau_{ex}(d_0)}{\partial x} \quad (3.7)$$

It is important to note that the first order coupling change denoted as  $\frac{\partial \tau_{ex}(d_0)}{\partial x}$  is proportional to the reactive coupling coefficient. Assuming the mechanical displacements are on a much longer time scale than the light fields such that the intracavity light can adiabatically respond to the mechanical resonator, and the intracavity cross coupling is negligible ( $\mu = 0$ ), then the intracavity field amplitudes can be expressed as

$$a_{cw} = i \frac{s_{in}^1}{\sqrt{\tau_{ex}(d_1)}} \frac{1}{i(\Delta + g_{om}x) + \frac{1}{2\tau_0} + \frac{1}{\tau_{ex}(d_0)}} \quad (3.8)$$

$$a_{ccw} = i \frac{s_{in}^2}{\sqrt{\tau_{ex}(d_2)}} \frac{1}{i(\Delta + g_{om}x) + \frac{1}{2\tau_0} + \frac{1}{\tau_{ex}(d_0)}} \quad (3.9)$$

Assuming the system is critically coupled, such that  $\tau_{ex}(d_0) = 2\tau_0$ , equations 3.6-3.9 can be substituted into equations 3.4-3.5 and the transmitted light through each waveguide can be expressed as

$$s_{out}^1 = s_{in}^1 \left( 1 - \frac{i}{2\tau_0 \left( i\Delta + \frac{1}{\tau_0} \right)} - \frac{g_{om}x}{2\tau_0 \left( i\Delta + \frac{1}{\tau_0} \right)^2} + \frac{ix}{4\tau_0^2 \left( i\Delta + \frac{1}{\tau_0} \right)} \frac{\partial \tau_{ex}(d_0)}{\partial x} \right) \quad (3.10)$$

$$s_{out}^2 = s_{in}^2 \left( 1 - \frac{i}{2\tau_0 \left( i\Delta + \frac{1}{\tau_0} \right)} - \frac{g_{om}x}{2\tau_0 \left( i\Delta + \frac{1}{\tau_0} \right)^2} - \frac{ix}{4\tau_0^2 \left( i\Delta + \frac{1}{\tau_0} \right)} \frac{\partial \tau_{ex}(d_0)}{\partial x} \right) \quad (3.11)$$

The resulting light transmitted through the waveguides have three components. There is a constant field level from the input light source, a modulated field term proportional to the dispersive coupling coefficient, and a modulated field term proportional to the reactive coupling coefficient. Since the dispersive coupling coefficient is related to shifts in the cavity resonance, all waveguides coupled to the opto-mechanical resonator will experience the same (in-phase) modulation as a result. The reactive coupling, however, results in a light field modulation that depends on the local waveguide-resonator coupling behavior. Since the mechanical mode has been defined as having out-of-phase anti-nodal displacements, then the reactive coupling coefficient's resulting modulation terms on the transmitted light in equations 3.10 and 3.11 are also out-of-phase.

The transmitted light is again sent through a 3dB coupler, where the in-phase and out-of-phase components of the light are separated into the differential and common signals, which are then sent to the photodetectors. The expression for this transformation is similar to equation 3.1 and is expressed as

$$\begin{bmatrix} s_{PD}^1 \\ s_{PD}^2 \end{bmatrix} = \frac{1}{\sqrt{2}} \begin{bmatrix} 1 & i \\ i & 1 \end{bmatrix} \begin{bmatrix} s_{out}^1 \\ s_{out}^2 \end{bmatrix} \quad (3.12)$$

Another way to examine the behavior of this two-waveguide displacement detection scheme is to treat each waveguide as a port and each interaction as a transformation. While the 3dB coupler transformations have already been shown in equations 3.1 and 3.12, the waveguide-resonator interactions in equations 3.10 and 3.11 can be treated as a transformation such that  $\frac{s_{out}^1}{s_{in}^1} = T_{cav}^1$  and  $\frac{s_{out}^2}{s_{in}^2} = T_{cav}^2$ , where  $T_{cav}^k$  is a coefficient of the waveguide-resonator transformation matrix. The full matrix representation for the system is given as

$$\begin{bmatrix} s_{PD}^1 \\ s_{PD}^2 \end{bmatrix} = \frac{1}{2} \begin{bmatrix} 1 & i \\ i & 1 \end{bmatrix} \begin{bmatrix} T_{cav}^1 & 0 \\ 0 & T_{cav}^2 \end{bmatrix} \begin{bmatrix} 1 & i \\ i & 1 \end{bmatrix} \begin{bmatrix} s_{in} \\ 0 \end{bmatrix} \quad (3.13)$$

The differential (diff) and common (comm) signal amplitudes at the photodetectors in terms of the opto-mechanical coupling coefficients are

$$(diff) \quad s_{PD}^1 = s_{in} \left( \frac{ix}{4\tau_0^2 \left(i\Delta + \frac{1}{\tau_0}\right)} \frac{\partial \tau_{ex}(d_0)}{\partial x} \right) \quad (3.14)$$

$$(comm) \quad s_{PD}^2 = is_{in} \left( 1 - \frac{i}{2\tau_0 \left(i\Delta + \frac{1}{\tau_0}\right)} - \frac{g_{om}x}{2\tau_0 \left(i\Delta + \frac{1}{\tau_0}\right)^2} \right) \quad (3.15)$$

The differential signal (equation 3.14) only has the RF signal proportional to the reactive coupling coefficient, whereas the common signal (equation 3.15) contains both DC signal and RF from the dispersive coupling coefficient. In addition to distinguishing between the path-length change of the dispersive coupling and gap change of the reactive coupling, this displacement detection scheme can allow for

selective transduction of certain mechanical modes based on the resonant mode shape.

## **3.2 Selective Transduction of Mechanical Wineglass Modes in Silicon**

The previously mentioned opto-mechanical differential displacement detection scheme is applied to the wine glass modes of an on-chip integrated silicon mechanical resonator. By utilizing two orthogonal waveguides for optomechanical sensing at the anti-nodes of the 22.3 MHz wine glass mode, the phase difference between the wine glass modes can be used to selectively sense the desired wine glass modes as compared to other modes. This can pave the way for using wine glass modes for lower phase noise optomechanical oscillators.

### **3.2.1 Design of Mechanical Wineglass Modes**

The silicon mechanical resonators were designed using a silicon on insulator (SOI) platform with a thin device layer (220nm) using an established fabrication process (see appendix). The dimensions of the ring resonator were based on several design considerations. First, the mechanical modes of interest (wineglass) were designed for the range of 20-30 MHz to operate at low frequencies, but just above the noise signature of the Santec laser source used in the experimental setup. The frequencies of the wineglass modes are determined by the outer radius and width of the ring [27]. Figure 3.2 shows the geometry and COMSOL mode shapes of two generations of designs.

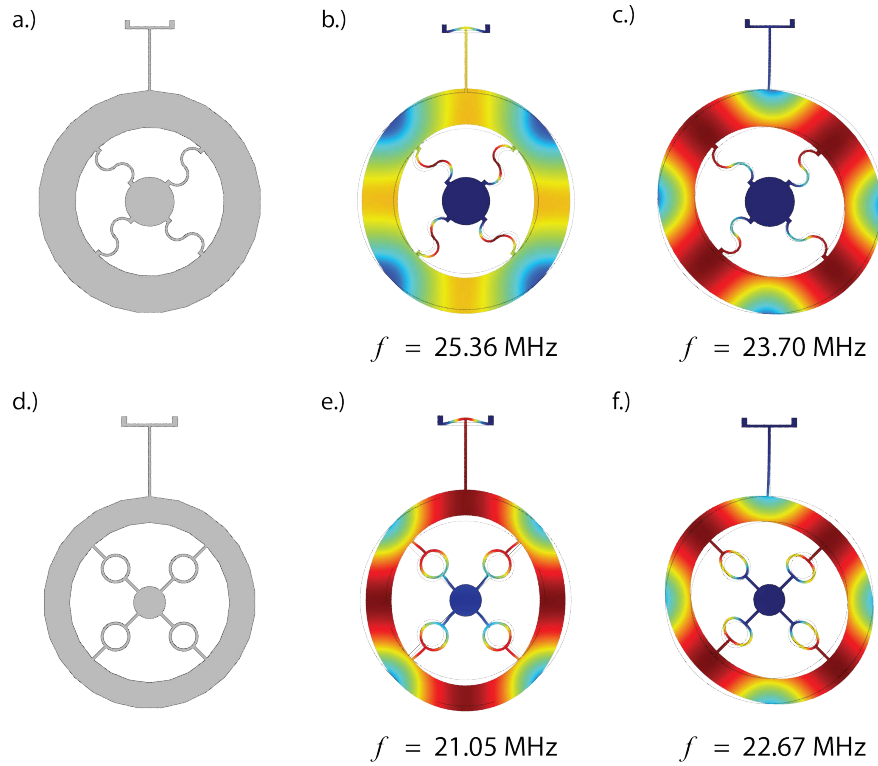


Figure 3.2: Wineglass mode ring resonator designs. Images (a-c) show the first generation resonator design and its non-degenerate wine-glass mode shapes and corresponding frequencies. Images (d-f) show the second generation ring design and corresponding mode shapes.

For the first generation of devices (image (a-c) in figure 3.2), the outer radius is  $18\mu\text{m}$  and the ring width is  $6\mu\text{m}$ . Since these devices are in the (100) crystal orientation, the anisotropy of the Si crystal lattice creates a non-degenerate set of wineglass modes with mode frequency splitting on the order of MHz [28, 29]. For certain applications, minimal frequency splitting is desired, so the anchoring scheme had to be carefully designed. It has been shown that the mechanical quality factor can be increased by reducing the number of anchoring points [30], but this opto-mechanical resonator design requires at least 5 anchoring points. As shown in the first generation designs, four anchoring spokes are required inside the ring. Since each wineglass mode has four nodes and anti-nodes, four spokes are needed to maintain the symmetric mode shapes needed for the differential balanced sensing. A fifth spoke is needed to ground the resonator so it can be electrostatically driven through capacitive forces. The spokes were designed in an S-shape to make them compliant and hence reduce the mode splitting [31].

The second generation designs (images (d-f) in figure 3.2) were meant to correct issues in the first generation designs. The ring width was reduced to  $3.7\mu\text{m}$  to account for changes in the tuning waveguide designs (discussed in later sections), which meant the outer radius had to be reduced to  $15\mu\text{m}$  to maintain the 20MHz wineglass resonance. The S-shaped spoke design was not entirely symmetric, as it created a net torque in one wineglass mode (image (b) in figure 3.2), which would lead to error in the waveguide-resonator coupling points. To resolve this, circle spokes were used, which are still compliant while being symmetric for both wineglass modes.

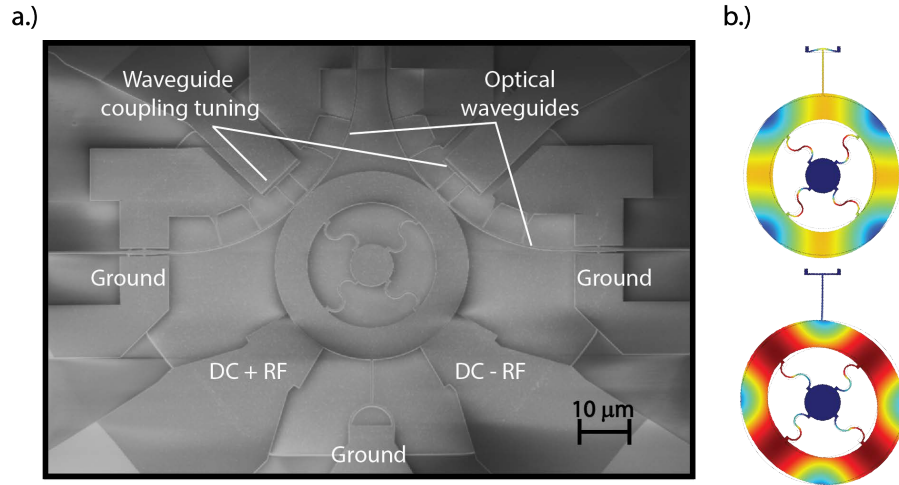


Figure 3.3: SEM of the first generation resonator with direct differential electrostatic drive (a). The ring has an outer radius of  $18\mu\text{m}$ , inner radius of  $12\mu\text{m}$ , and base radius of  $4\mu\text{m}$ . The resonator-waveguide gap is  $80\text{nm}$  and resonator-electrode gap is  $100\text{nm}$ . The optical waveguide tuning capacitor gap is  $150\text{nm}$ . Wine-glass mode shapes of first generation devices are shown in (b) with same frequencies as Figure 3.2 (b-c).

### 3.2.2 Electrode Design for Electrostatic Drive

In order for the differential opto-mechanical sensing scheme to be experimentally characterized, the non-degenerate wineglass modes must be excited to create displacement for readout. A convenient method for exciting mechanical resonances in silicon is through electrostatic capacitive forces. Figure 3.3 shows an SEM of the first generation electrode design. The two  $30^\circ$  electrodes are placed at orthogonal anti-nodes of the desired wineglass mode. While the overlap between the electrodes and the mechanical wineglass modes is sufficient for driven oscillations, the overlap with the resonator's optical modes creates significant optical loss. This increase in optical loss causes a decrease in intrinsic optical quality factor (smaller  $\tau_0$ ) Therefore, the introduction of electrodes near the opto-mechanical resonator changes the critical coupling condition, now requiring a smaller coupling rate  $\tau_{ex}$ , which can be

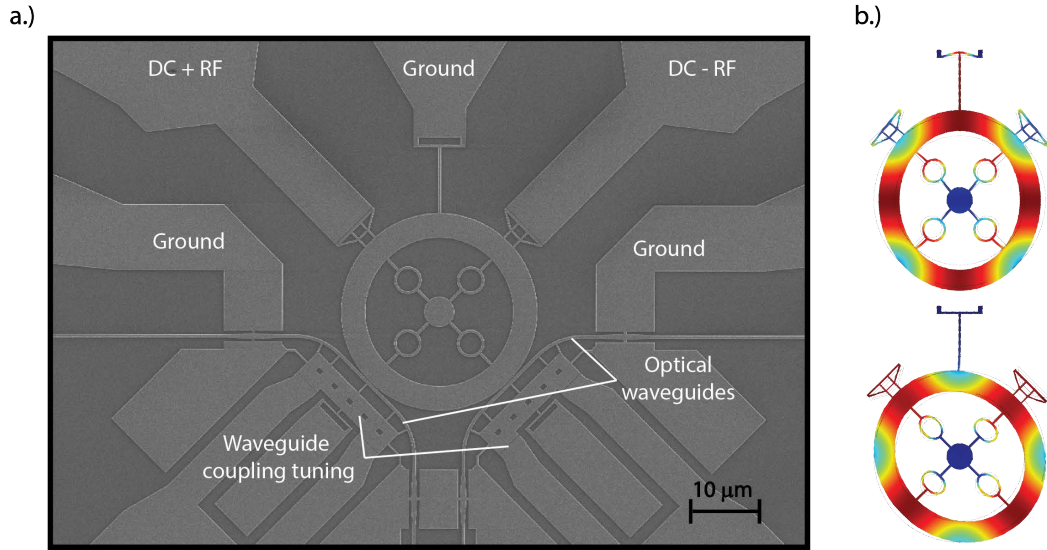


Figure 3.4: SEM of the second generation resonator with attached differential electrostatic drive (a). The ring has an outer radius of  $15\mu\text{m}$ , inner radius of  $11.3\mu\text{m}$ , and base radius of  $2.3\mu\text{m}$ . The resonator-waveguide gap is  $90\text{nm}$  and resonator-electrode gap is  $100\text{nm}$ . The optical waveguide tuning capacitor gap is  $100\text{nm}$ . Wineglass mode shapes of modified second generation devices are shown in (b) with resonant frequencies of  $20.99\text{ MHz}$  (top) and  $21.91\text{ MHz}$  (bottom).

achieved by reducing the waveguide-resonator gap [32]. Due to e-beam lithography fabrication limitations, achieving critical coupling with this electrode design is highly impractical.

For the second generation devices, two different electrode designs were considered to minimize the optical loss from the electrodes while maintaining the same overlap (drive efficiency) with the mechanical resonance. Figure 3.4 shows an SEM of the electrodes attached to the opto-mechanical resonator. This design pushes the electrode-resonator gap farther away from the optical modes, reducing the optical losses from the silicon. The optical modes now only see four scattering points instead of large strips of silicon. The drawback to this design is the asymmetric

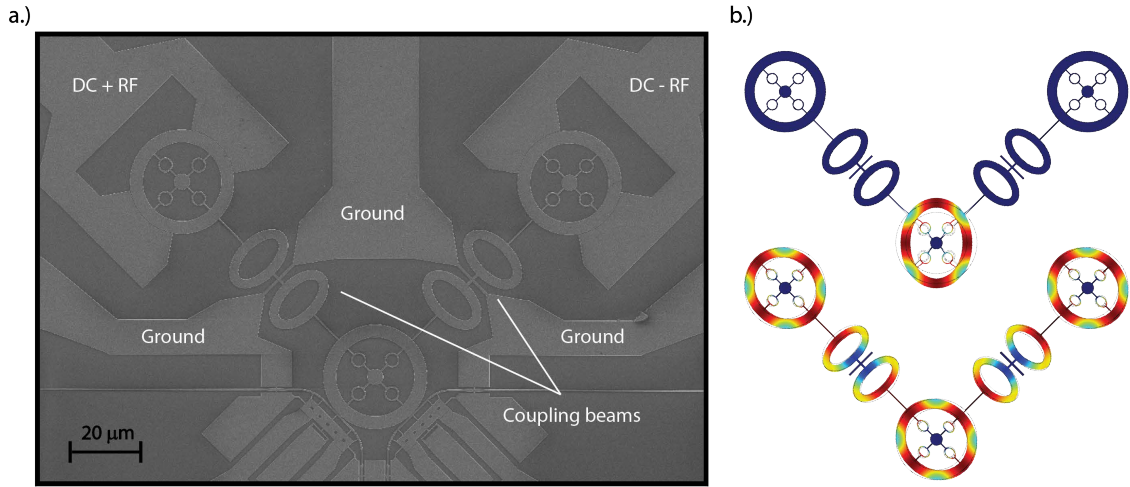


Figure 3.5: SEM of the second generation resonator with 2-coupled-ring differential electrostatic drive (a). The ring has an outer radius of  $15\mu\text{m}$ , inner radius of  $11.3\mu\text{m}$ , and base radius of  $2.3\mu\text{m}$ . The coupling beams are a modified  $\lambda/2$  design with a length of  $47\mu\text{m}$ . The resonator-waveguide gap is  $90\text{nm}$  and resonator-electrode gap is  $100\text{nm}$ . The optical waveguide tuning capacitor gap is  $100\text{nm}$ . Wineglass mode shapes of modified second generation devices are shown in (b) with resonant frequencies of  $20.68\text{ MHz}$  (top) and  $22.70\text{ MHz}$  (bottom).

mass loading from the attached electrodes. As discussed in later chapters, this mass loading can create asymmetric displacements at the anti-nodes and shift the position of maximum displacement for the modes of interest.

The last design for the second generation devices aims to geometrically separate the optical and electrostatic components through a coupled ring architecture [33]. Figure 3.5 shows an SEM of the 3-coupled-ring design. The two outer rings are driven (differentially) through electrostatic forces and the displacements are coupled to the central optical cavity through  $\lambda/2$  coupling beams [33]. These coupling beams were designed for the wineglass mechanical modes. There are three advantages to this driving scheme over the previous electrode designs. Optically,

there are only two scattering points from the two coupling beams, which reduces the optical loss and makes critically coupling to the optical mode manageable. Mechanically, there is no mass loading or distortion of the wineglass modes from the coupling beams. Also, due to the coupling beam design, the driven non-degenerate wineglass modes are decoupled (image (b) in figure 3.5). This means only the wineglass mode of interest can be driven electrostatically while the other wineglass mode won't couple to any of the drive ring displacements.

### 3.2.3 Optical Coupling Design and Phase Matching

In order to optically detect the electrostatically driven displacement, the waveguide-resonator coupling region must be carefully designed. In order to achieve the critical coupling condition, the optical coupling coefficient must be large enough to match the intrinsic optical losses [32]. The general expression for the coupling coefficient is [34]

$$\kappa = \frac{i\omega\epsilon_0}{4} \int_{-\infty}^{\infty} \int_0^W \int_0^h (n_{Si}^2 - 1) E_{disk} \cdot E_{wg} e^{j\phi} dy dx dz \quad (3.16)$$

where  $W$  is the waveguide width,  $h$  is the silicon device layer height,  $n_{Si}$  is the refractive index of silicon,  $E_{disk}$  and  $E_{wg}$  are the normalized electric field component of the resonator and waveguide optical modes, respectively, and  $\phi$  is the phase mismatch between the optical modes. As seen in equation 3.16, two major factors that allow for a large optical coupling coefficient are the mode overlap integrals and phase mismatch. The overlap between the optical waveguide and resonator modes can be controlled by adjusting the waveguide-resonator gap. In order to achieve critical coupling for a released waveguide-resonator system with a reasonable gap,

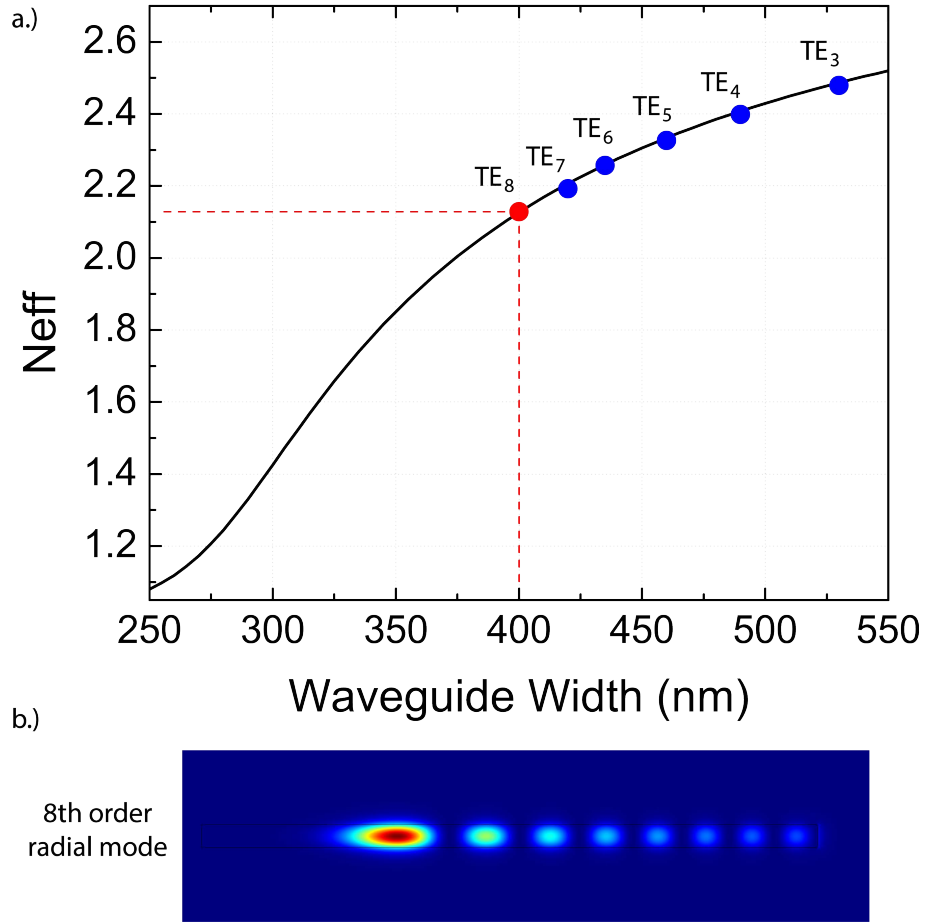


Figure 3.6: Plot (a) shows the effective index of the waveguide mode (translated to the disk edge) as a function of waveguide width assuming a gap of 90 nm. The effective index of several TE radial modes for first generation devices are marked as points on the curve, corresponding to waveguide widths for achieving phase matching at 1550 nm. First generation devices were phased matched to the 8th radial order TE mode with the  $|E_r|^2$  profile given in (b).

the phase mismatch must be minimized [32, 34]. The phase term in equation 3.16 can be approximated as [34]

$$\phi = k_0 z (n_{wg} - n_{disk} \zeta) \quad (3.17)$$

where  $k_0 = 2\pi/\lambda_0$  is the wavenumber of the optical mode,  $n_{wg}$  is the effective index of the waveguide mode,  $n_{disk}$  is the effective index of the resonator mode, and  $\zeta$  is a factor in terms of the waveguide width ( $W$ ), waveguide gap ( $d$ ), and resonator radius ( $R$ ). The waveguide effective index can be expressed in terms of the mode's propagation constant ( $\beta_{wg}$ ) as  $n_{wg} = \beta_{wg}/k_0$ . The resonator's effective index at the outer radius edge is defined as  $n_{disk} = m/k_0 R$ , where  $m$  is the azimuthal mode order. The geometric factor can be defined as  $\zeta = \frac{R}{R+d+W/2}$ . By solving for the minimum of equation 3.17, the phase matching condition is [34]

$$n_{disk} = \frac{n_{wg}}{\zeta} \quad (3.18)$$

Given the resonator's optical TE polarized mode of radial order  $p$  ( $TE_p$ ), the waveguide's effective index can be matched to that of mode  $TE_p$  by adjusting the waveguide's width. Therefore, given a plot of the waveguide's effective index translated to the disk edge versus the waveguide width ( $n_{wg}/\zeta$  vs.  $W$ ), the waveguide width needed for phase matching to a given resonator mode can be found. Using COMSOL to determine the effective indices of the waveguide and resonator modes, figure 3.6 shows the phase matching plot for the first generation resonator design. Since there are scattering points from the spokes on both the inside and outside of the ring resonator, the optical mode chosen for phase matching was one that did not see the inside of the ring and had a very low field amplitude at the

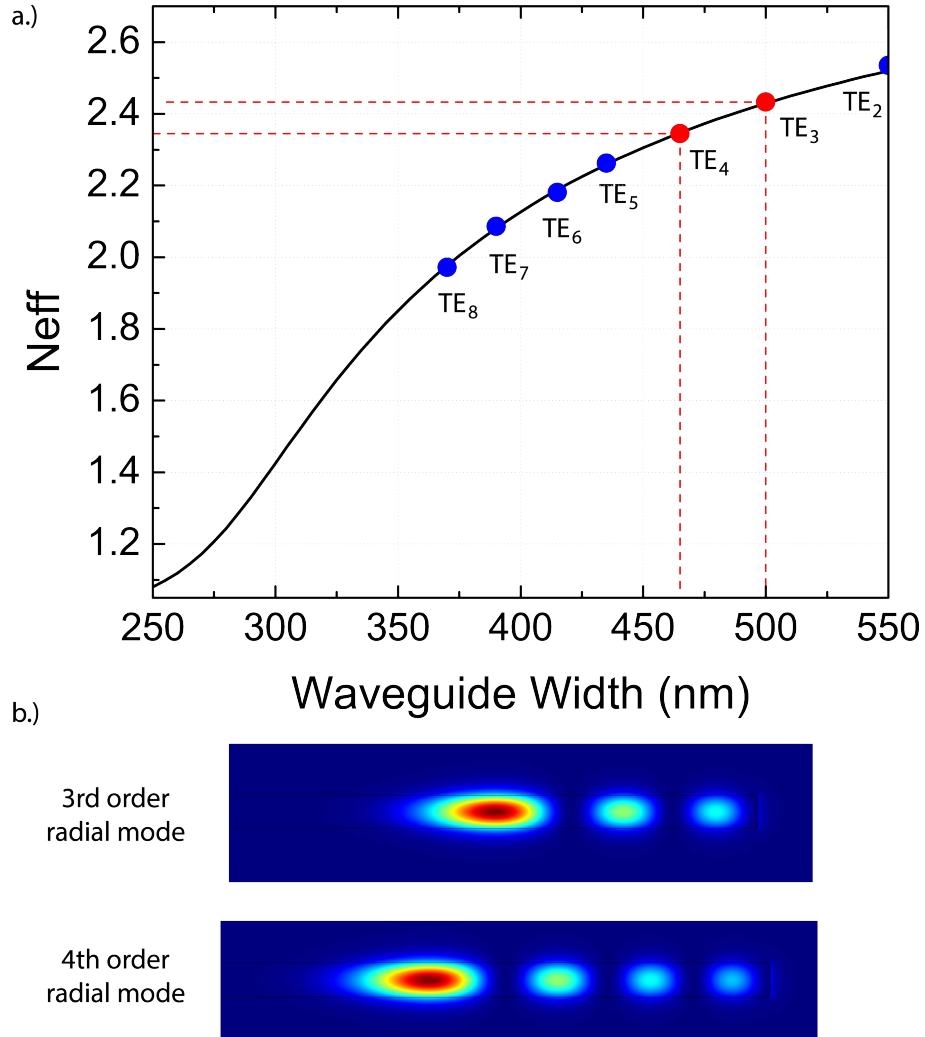


Figure 3.7: Plot (a) shows the effective index of the waveguide mode (translated to the disk edge) as a function of waveguide width assuming a gap of 90 nm. The effective index of several TE radial modes for second generation devices are marked as points on the curve, corresponding to waveguide widths for achieving phase matching at 1550 nm. Second generation devices were phased matched to the 3rd and 4th radial order TE modes with the  $|E_r|^2$  profiles given in (b).

ring edge. For the first generation devices, a waveguide width of 400nm was chosen to match to the eight order radial optical mode, whose  $E$  field profile is shown in image (b) of figure 3.6.

Similarly, figure 3.7 shows the phase matching plot for the second generation ring design. Here, because the ring width is smaller than the first generation design, the eight order radial mode has a large field amplitude at the inside of the ring. Therefore, lower order radial modes were chosen for phase matching. For the second generation devices, waveguide widths of 470nm and 500nm were chosen to phase match to the third and fourth order radial modes ( $E$  field profiles shown in image (b) of figure 3.7).

### 3.2.4 Electrostatically Tunable Waveguides

In order to achieve balanced differential displacement detection, not only do the displacements at the coupling points need to be equal, but the reactive coupling coefficients must also be equal. Since the coupling coefficient is proportional to  $\frac{\partial \tau_{ex}(d_0)}{\partial x}$ , then the waveguide-resonator gaps  $d_0$  must be equal. Due to fabrication errors, the gaps will be unequal which means a tuning element is needed. Tuning of optical waveguides has been demonstrated [35] and in this device, electrostatic tuning based on a simple gap-closing capacitor will be implemented. In the first generation of devices, only one form of tunable waveguide was designed. With the application of DC voltage, the waveguide moved farther away from resonator (negative tuning). The second generation devices not only had an improved negative tuning design, but a positive tuning design was implemented using a mechanical level system to move the waveguide closer to the resonator with a DC voltage. Figure 3.8 is a graph of the waveguide DC displacement profiles for all three designs.

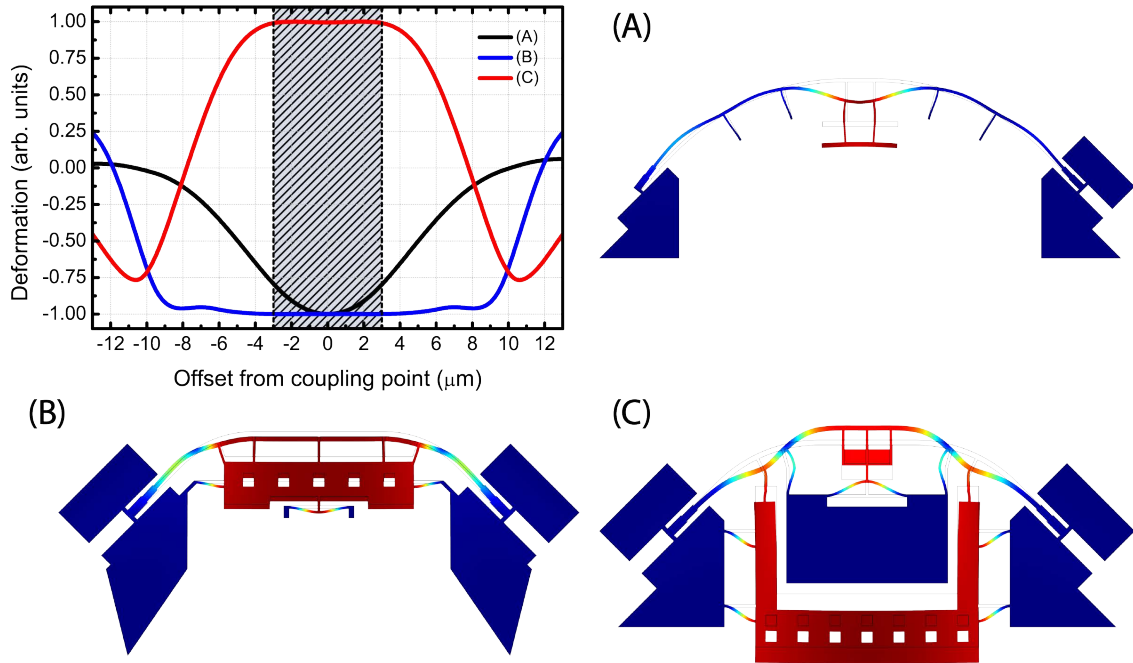


Figure 3.8: The deformation profile along the waveguide for all three waveguide tuning designs are compared in the graph above. The shaded graph region is the approximate coherent coupling length of a point coupled waveguide to a traveling wave resonator (TWR). The shapes of the statically displaced waveguides are shown in (A) for the first generation, and (B-C) for the second generation.

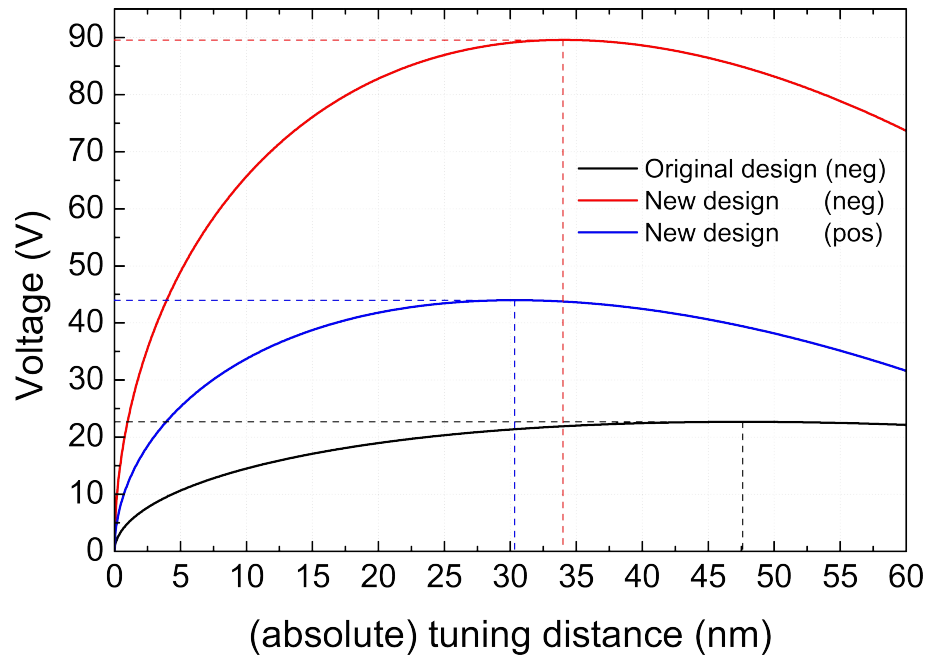


Figure 3.9: Graph of the DC voltage applied across the tunable waveguide vs. waveguide gap change at the coupling point. Pull-in of the tuning element limits the maximum tuning range and voltage that can be applied (marked as dashed lines). Negative tuning (neg) refers to moving the waveguide away from the resonator and positive tuning (pos) moves the waveguide toward the resonator.

When trying to obtain equal coupling coefficients, not only do the waveguide gaps need to be equal, but the phase mismatch between the waveguide and resonator modes must also be equal. To ensure the same phase matching condition as the gap is changed, the waveguide must maintain its flat shape (point coupling) over the effective coupling length. The first generation tunable waveguide (image (A) in figure 3.8) does not remain flat over the coupling length, which can severely limit its effective tuning range as the two waveguides have different phase matching conditions. The second generation negative and positive tuning designs (images (B) and (C) in figure 3.8, respectively) both retain their shape over the effective coupling length, allowing for a large tuning range.

The performance of these tunable waveguides (voltage applied vs. waveguide displacement) is simulated and shown in figure 3.8 for all three tuning designs. The tuning range limits are obtained from the pull-in characteristics of the gap-closing capacitor. The pull-in voltage is defined as [36]

$$V_{PI} = \sqrt{\frac{8K_{eff}d_0^3}{27\varepsilon_0A_{eff}}} \quad (3.19)$$

where  $K_{eff}$  is the effective spring constant,  $\varepsilon_0$  is the permittivity of free space, and  $A_{eff}$  is the effective area. The gap at which pull-in occurs is one-third of the original gap ( $d_{PI} = d_0/3$ ) [36]. In figure 3.9, the first generation tunable waveguides had a starting gap of  $d_0 = 150\text{nm}$ , whereas the second generation designs had a starting gap of  $d_0 = 100\text{nm}$ . The gap was reduced to lower the pull-in voltage. The voltage levels are higher for the second generation designs because the effective spring constant had to be increased to maintain the waveguide's shape in the coupling region. Overall, the maximum tuning for the second generation waveguide designs were maintained between 30-35nm with maximum voltages of

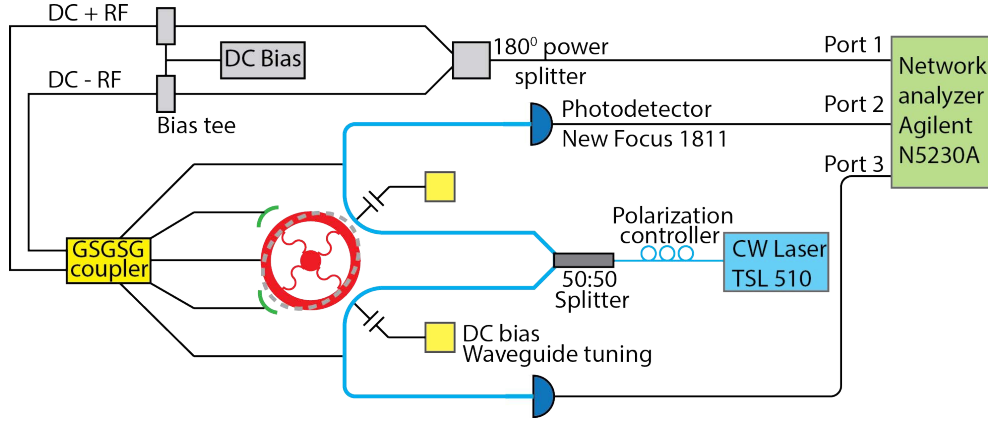


Figure 3.10: Schematic of the differential drive and sense experimental setup.

less than 100V are needed.

### 3.2.5 Experimental Characterization

The selective transduction of mechanical wineglass modes was experimentally characterized for the first generation device designs. Figure 3.10 is an illustration of the experimental setup. For RF transmission measurements, a DC bias is added to the RF output from Port 1 of the network analyzer and used to drive the  $n=2$  wineglass mode of the resonator (grey dotted line). Two optical waveguides couple light from a continuous wave laser into the resonator. The mechanical motion modulates the light and its amplitude and phase is measured using photodetectors on port 2 and 3 of the network analyzer. It is possible to tune the coupling of the optical waveguide to the resonator through the application of a DC bias on the tunable waveguides.

Figure 3.11 shows plots of optical resonance from the first generation devices. Plot (a) of figure 3.11 is an example optical resonance with the measured data (blue) and Lorentzian curve fit (red). The loaded optical quality factor was 95k and

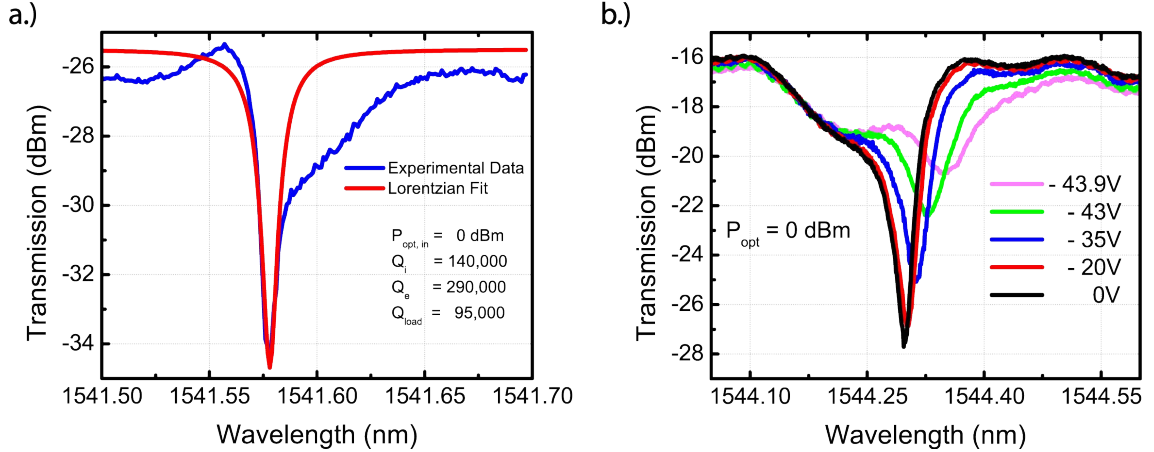


Figure 3.11: Plot (a) shows an optical resonance measured on the first generation devices with a loaded optical  $Q$  of 95k. Plot (b) shows the tuning of the coupling to another optical resonance of the resonator by changing the resonator-waveguide gap using a gap change capacitor (first generation device and waveguide tuning).

the resonance was undercoupled but near critical coupling. With an input optical power of 0dBm, the total loss through the system was 26dB, which comes from the insertion loss of the grating couplers, the 3dB splitter, and optical connectors between the splitter and polarization controller.

Plot (b) of figure 3.11 is a demonstration of tuning the optical coupling for a different optical resonance. First, the optical resonance was measured With an initial voltage of 0V applied to the DC bias pads of the tunable waveguide (black). Then, as the magnitude of the applied voltage increased, the waveguide was pulled farther away from the resonator. Since the resonance was initially undercoupled, increasing the waveguide gap would further undercouple the resonance. With an applied voltage of -43.9V (pink), the resonance is almost completely undercoupled with a total reduction of 7dB in the extinction ratio. There is, however, a significant shift (70pm) in the optical resonance. This shift is caused by the presence of the waveguide perturbing the cavity's resonance. As the shape of the waveguide

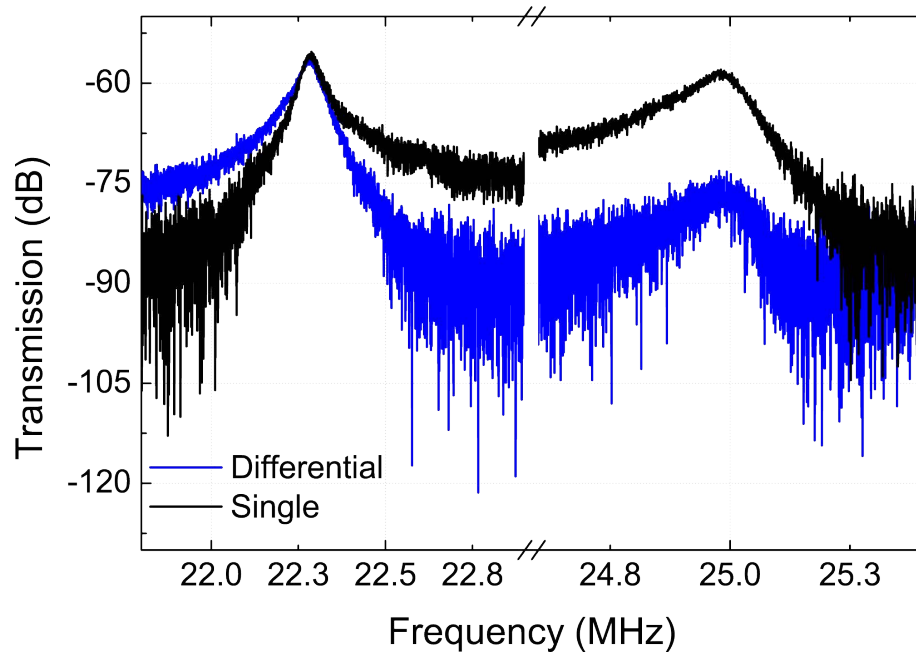


Figure 3.12: For a first generation device, the amplitude of the  $n=2$  wine-glass modes for single-ended (black) and differential (blue) electrostatic drive measured using optical waveguide on port 2. The electrodes are designed to favorably drive the  $45^\circ$ - $135^\circ$  (22.3MHz) mode. Measurements were carried out with input optical power of 11.5dBm at 1528nm, input RF power of -5dBm (-2dBm) for single-ended (differential) drive with a DC bias of 12V.

is deformed through tuning, it changes its perturbation of the optical resonance, leading to a new resonance condition and therefore a shift from the previous resonance.

The drive electrodes for the first generation design are capable of driving the wineglass modes either differentially (as shown in figure 3.10) or through a single drive electrode by disconnecting one RF signal after port 1's power splitter. Figure 3.12 shows a comparison of the RF transmission spectrum for both  $n=2$  wineglass modes with differential and single RF drive. For the wineglass mode of interest (22.3 MHz mode), the differential drive is in-phase with the anti-nodes, allowing for favorable excitation. The other wineglass mode (25 MHz mode) is symmetric with respect to the drive electrodes, so the differential drive is out-of-phase with the mechanical mode. This results in over a 15dB reduction in signal amplitude for the 25 MHz mode when using differential electrostatic drive. This differential driving scheme can selectively drive the wineglass mode of interest while reducing the drive efficiency of the other wineglass mode.

Now, using single-ended electrostatic drive for the first generation devices, the RF transmission of both wineglass modes is compared at ports 2 and 3. Figure 3.13 has the amplitude and wrapped phase of the RF transmission at ports 2 and 3. From the amplitude plots (top), the magnitude of the displacement signals are not balanced at the waveguide outputs. Therefore, a differential detector can not be implemented until the signals are balanced. The waveguide tuning needs to be more stable to successfully achieve balanced differential displacement detection. The phase information (bottom) confirms the principle behind the differential detection scheme. For the wineglass mode of interest (plots (a) in figure 3.13), the output RF signals are out of phase, indicating that the reactive coupling coefficient at the two

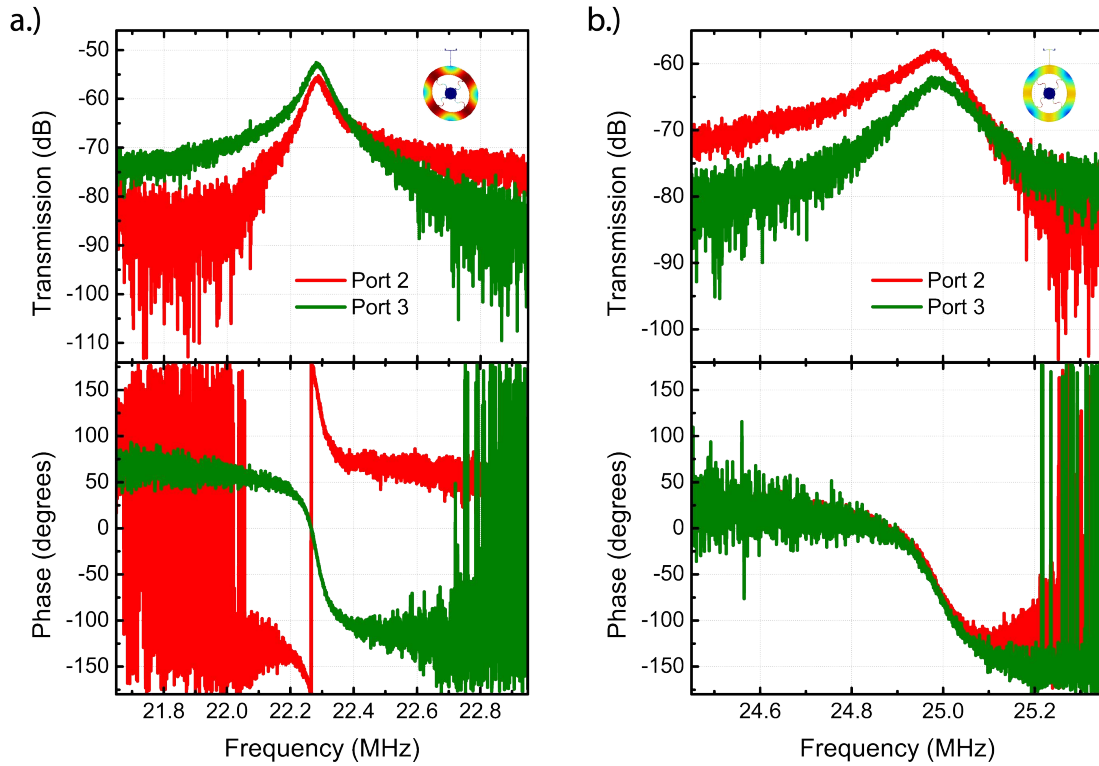


Figure 3.13: For the same first generation device, plots show the amplitude (above) and phase (below) of the single-end driven  $45^\circ$ - $135^\circ$  (a) and  $0^\circ$ - $90^\circ$  (b)  $n=2$  wineglass modes measured by the two optical waveguides on port 2 (red) and port 3 (green). The optical waveguides are positioned at the anti-nodes (nodes) of the  $45^\circ$ - $135^\circ$  ( $0^\circ$ - $90^\circ$ ) mode and hence at the respective resonances show a  $180^\circ$  ( $0^\circ$ ) difference in the signal phase. Inset shows COMSOL simulations of the respective modes. Measurements were done with input optical power of 11.5 dBm at 1528nm, input RF power of -5dBm and a DC bias of 12V.

coupling points generated out-of-phase RF modulation. The other wineglass mode shape (plots (b) in figure 3.13) is symmetric with respect to the waveguide coupling points, so the reactive coupling should generate in-phase modulation. This results in RF output signals that are in-phase, which can be suppressed with the use of a differential photodetector.

### 3.3 Silicon MEMS Wineglass Gyroscope with Differential Optical Coriolis Sensing

With a differential displacement detection scheme that is selective to one of several orthogonal modes, one application would be a vibratory gyroscope for sensing coriolis acceleration. To make a high frequency vibratory gyroscope in the range of 20-50 MHz, a mode family of at least two orthogonal modes is needed. Here, the designed 20 MHz n=2 wineglass modes from the previous section can be used. When the mechanical resonator is in the presence of an external rotation relative to its reference frame, a coriolis acceleration is generated as [37]

$$\vec{a}_{coriolis} = -2\vec{v} \times \vec{\Omega} \quad (3.20)$$

where  $\vec{v}$  is the velocity of the resonator and  $\vec{\Omega}$  is the applied rotation. From equation 3.20, one can see that the acceleration that arises from rotation acts orthogonal to the resonator's velocity. In the case of a vibratory gyroscope operating with the n=2 wineglass modes, one mode is used as the "drive mode" and the other as the "sense mode". The drive mode is excited and with the introduction of rotation induces oscillations in the sense wineglass mode. The sensing scheme

then measures this displacement, which is proportional to the applied rotation.

When energy is coupled to the sense mode, it is at the drive mode frequency. Therefore, to maximize the displacement at the sense and get the full enhancement of the sense modes mechanical quality factor, the drive and sense modes should be very close in resonant frequency. The following section will discuss the design adjustments to the ring resonator to reduce the wineglass mode splitting. Then, initial COMSOL simulations will investigate the behavior of these ring resonators as potential vibratory gyroscopes.

### **3.3.1 Adjusted Ring Design to Reduce Mode Splitting**

The ring resonator designs with four spokes in the previous sections had MHz splitting in the wineglass modes. To reduce the mode splitting, the circle spoke design is used to counteract the anisotropic nature of the single crystal silicon. Since the effective spring constant of each circle spoke is proportional to the circle's radius, then each wineglass mode will have a set of four spokes where the radius of the spokes will set each modes resonant frequency. Figure 3.14 shows the images of the second generation resonator designs with adjusted mode splitting. For example, in the 2-coupled-ring design (images (d-f) of figure 3.14), the drive mode has spokes with radius of  $2.12\mu\text{m}$  and the sense mode has spokes with radius of  $1.75\mu\text{m}$ . This means due to silicon's anisotropy, the drive mode is higher frequency than the sense mode. Therefore, the drive mode's spokes had a larger radius than the sense spokes to reduce the drive frequency relative to the sense frequency. This increase from four to eight circle spokes reduced the mode splitting from 2MHz to 76kHz.

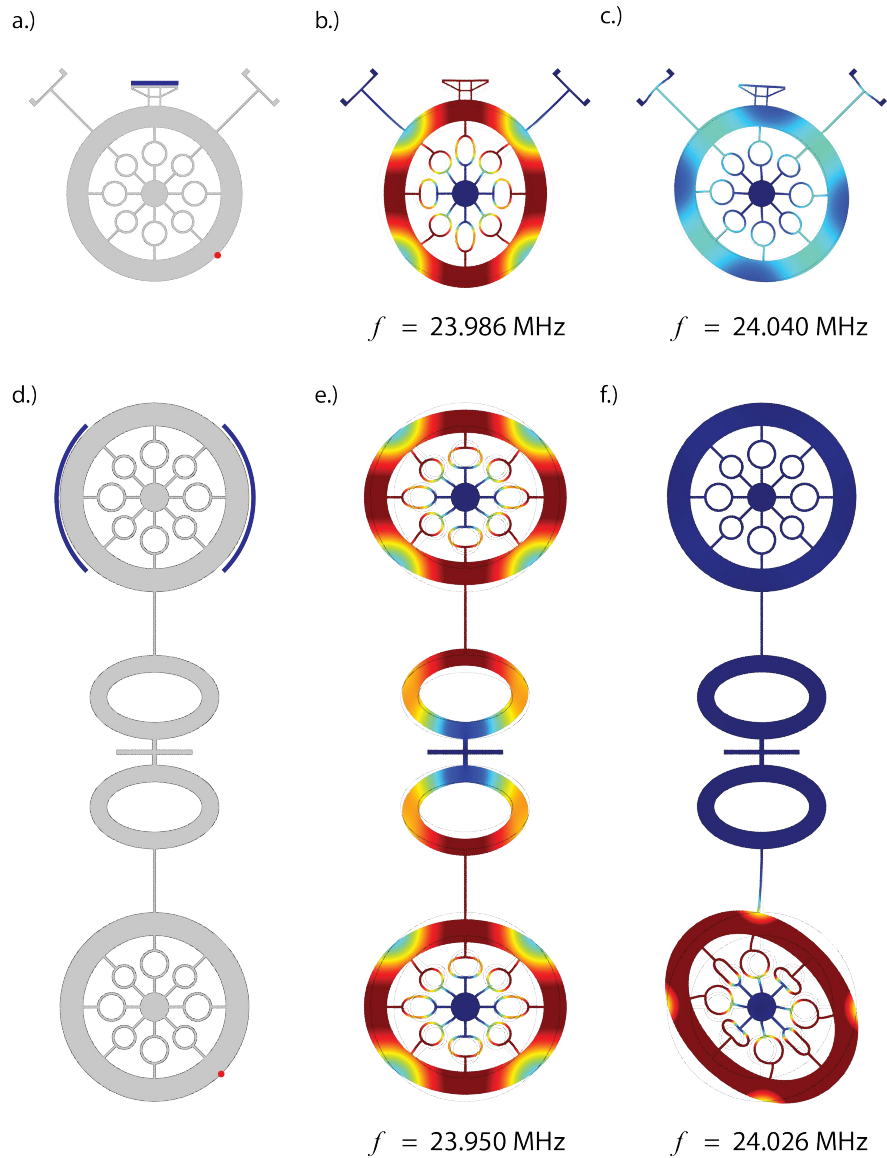


Figure 3.14: Second generation wineglass resonator designs had additional spokes added with unequal circle springs to reduce the mode splitting from the anisotropic nature of single crystal Silicon. For an attached electrode driving scheme (a-c), the circle springs had radii of  $1.8\mu\text{m}$  and  $2\mu\text{m}$ . From COMSOL simulations, The frequency split was reduced to 54kHz. For a 2-coupled-ring electrode driving scheme (d-f), the circle springs had radii of  $1.75\mu\text{m}$  and  $2.12\mu\text{m}$ . From COMSOL simulations, The frequency split was reduced to 76kHz. For initial COMSOL simulations to model the effect of coriolis force, the "drive" wineglass mode was actuated (blue lines) and the displacement of the "sense" wineglass mode was examined (red dot).

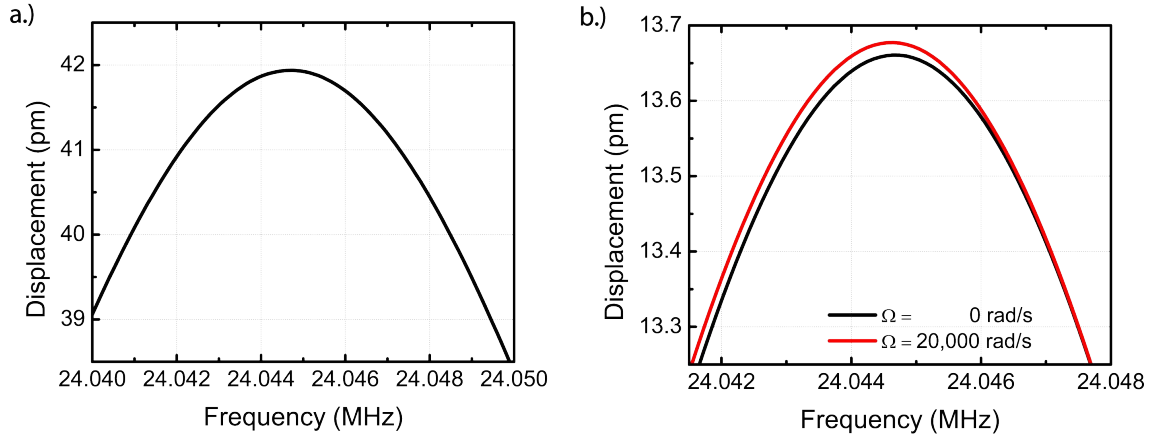


Figure 3.15: For the attached electrode driving scheme, plot (a) shows the displacement of the driven wineglass mode at one of its anti-nodal points. The displacement at the sense wineglass mode’s anti-nodal point (b) is compared with and without rotation present (coriolis force).

### 3.3.2 Modeling of Coriolis Force Displacements

To demonstrate the viability of the resonator designs in figure 3.14 as vibratory gyroscopes, simulations with external rotations were performed in COMSOL. For the two resonator designs, the drive wineglass modes were actuated along the blue curves in figure 3.14. Rotation rates of 0 rad/s and 20,000 rad/s were applied and the maximum of both the drive and sense modes were plotted verse frequency.

The results of the simulations for the attached electrode resonator design are shown in figure 3.15. In the absence of rotation, there is not only a displacement at the drive anti-nodes, but also at the sense anti-nodes. While the nodal points of the drive mode are at the sense locations, the nodal points aren’t entirely stationary, leading to an error signal at the sense locations. Therefore, the sense signal from the applied rotation is the measured displacement above this error signal from the drive mode. Plot (b) in figure 3.15 shows the sense displacement with and without

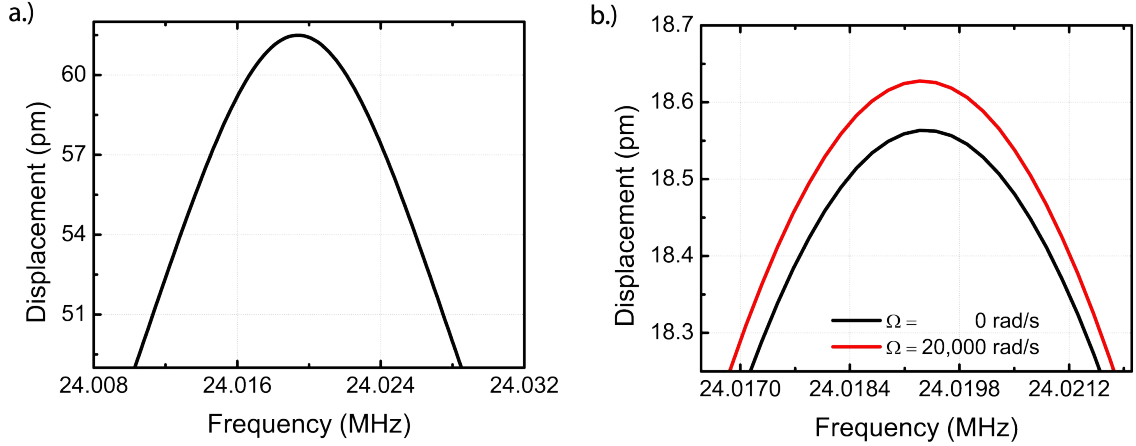


Figure 3.16: For the 2-coupled-ring electrode driving scheme, plot (a) shows the displacement of the driven wineglass mode at one of its anti-nodal points. The displacement at the sense wineglass mode’s anti-nodal point (b) is compared with and without rotation present (coriolis force).

rotation. Since there is an increase in the sense mode’s displacement in the presence of rotation, the resonator design is viable for use as a vibratory gyroscope.

Figure 3.16 shows the simulation results for the 2-coupled-ring design. With no rotation present, the drive and sense displacements are comparable to those of the attached electrode design. The sense displacement with rotation, however, is a much larger change than with the previous design. This is due to the asymmetric mass loading in the attached electrode design. The attached electrode causes a net torque on the sense mode, which means the drive and sense wineglass modes are not entirely orthogonal. This reduces the efficiency of coupling energy from the drive to sense mode and therefore making the change in sense displacement (with rotation) less than the coupled ring design.

## CHAPTER 4

### CONCLUSION AND FUTURE WORK

This thesis focused on taking established opto-mechanical sensing and driving schemes and incorporating them into MEMS oscillator and inertial sensor systems. First, the combination of radiation pressure induced oscillations and closed-loop RF feedback induced oscillations in an opto-mechanical resonator was investigated. While these oscillation mechanisms have been individually studied and characterized [19, 21], the simultaneous operation of these mechanisms in a silicon opto-acoustic oscillator resulted in a 10dB far-from-carrier phase noise improvement and increase in output signal power. Further work on this topic could try to push radiation pressure induced oscillations to higher frequencies, which could lead to demonstrating this combined driving scheme at GHz frequencies.

Opto-mechanical displacement sensing was incorporated into a electrostatically driven vibratory gyroscope design. A theoretical model was developed for a two-waveguide differential displacement detection scheme utilizing the reactive opto-mechanical coupling coefficient. Several resonators, drive electrodes, and DC bias tuning waveguides were designed to compare the performance of each. Initial experimental characterization was performed on the first generation devices. The second generation devices were modified for vibratory gyroscope applications with initial COMSOL simulations performed. Further work would include experimental characterization of the second generation designs. Then, by closing the loop on the electrostatic drive, demonstrate an oscillator with the differential sensing scheme (second generation devices). For the opto-mechanical gyroscope, the modified resonators must be fabricated, tested, and rotation rate measurements carried out to demonstrate the validity of a opto-mechanically sensed vibratory gyroscope.

APPENDIX A

**FABRICATION PROCESS FOR SILICON OPTO-MECHANICAL  
RESONATORS**

### **A.1 Process Flow for OAO Silicon Resonators**

The detailed fabrication process for the silicon opto-mechanical resonators used as an opto-acoustic oscillator can be found in appendix B of the thesis [38].

### **A.2 Process Flow for OMG Silicon Resonators**

These silicon opto-mechanical resonators were fabricated on silicon on insulator (SOI) wafers from Soitec. The 6 inch wafers have a (100) orientation with a 250nm thick high resistivity (10-20 ohm-cm) silicon device layer on a 3 $\mu$ m buried oxide (BOX) layer.

#### **A.2.1 List of Process Steps for Full Run**

##### **1. Measure SOI stack**

Equipment: FilMetrics F40/F50-EXR

Measure the initial stack height to establish the starting Si device layer and buried oxide thickness.

##### **2. MOS clean**

Equipment: MOS clean wet bench

Recipe: 10 minutes dip in 1:1:6 NH<sub>4</sub>OH:H<sub>2</sub>O<sub>2</sub>:H<sub>2</sub>O at 70°C

10 minutes dip in 1:1:6 HCl:H<sub>2</sub>O<sub>2</sub>:H<sub>2</sub>O at 70°C

Rinse in De-Ionized (DI) H<sub>2</sub>O

### **3. Grow thermal oxide : hard mask creation**

Equipment: MRL Industries furnace (Wet/Dry Oxide furnace - B2)

Recipe: 23 minutes at 900°C using wet HCl oxidation to obtain 50nm oxide hard mask.

### **4. Measure oxidized stack**

Equipment: FilMetrics F40/F50-EXR

Measure the stack height after thermal oxidation to establish the oxide hard mask layer, Si device layer, and buried oxide layer thicknesses.

### **5. Photo resist spin**

Equipment: Photo resist spinners

Recipe: Spin P20 primer with parameters:

(wait 10s before spinning)

Speed = 3000rpm, ramp = 1000 rpm/s, time = 30s

Spin SPR 220-3.0 photo resist with parameters:

Speed = 3000rpm, ramp = 1000 rpm/s, time = 30s

Hard bake at 115°C for 90s

### **6. Dice wafer**

Equipment: K&S 7100 Dicing Saw

Dice the 6 inch wafer into 2cm x 2cm square pieces.

### **7. Resist removal**

Equipment: General Chemistry hood

Recipe: 10 min acetone dip  
5 min isopropyl alcohol dip  
Rinse with DI H<sub>2</sub>O

## 8. Surface clean/preparation

Equipment: Acid chemical hood

Recipe: 2 minute dip in Nanostrip  
Rinse in DI H<sub>2</sub>O

## 9. E-beam resist spin

Equipment: E-beam resist spinner

Recipe: Spin Ma-N 2403 e-beam resist with parameters:

Speed = 5000rpm, ramp = 2000 rpm/s, time = 30s

Hard bake at 90°C for 1 minute

## 10. E-beam lithography

Equipment: JEOL JBX9500FS (JEOL 9500) e-beam lithography system

Recipe: Expose at 2nA with doses:

1000 $\mu$ C/cm<sup>2</sup> for waveguides

850 $\mu$ C/cm<sup>2</sup> for gratings

500 $\mu$ C/cm<sup>2</sup> for the resonators

550 $\mu$ C/cm<sup>2</sup> for the tunable waveguide supports

400 $\mu$ C/cm<sup>2</sup> for the electrical routing and probe pads

## 11. Develop e-beam resist

Equipment: Electron beam resist hood

Recipe: 75s in 726MIF developer

## **12. Resist height measurement**

Equipment: P-10 profilometer

Measure step height of the e-beam resist across alignment marks.

## **13. Descum after developing resist**

Equipment: Oxford PlasmaLab 80+ (Oxford 81/82) etcher

Recipe: Oxygen plasma clean on empty chamber, time = 10 minutes

Oxygen plasma clean recipe on sample, time = 9s

## **14. Oxide hard mask etch**

Equipment: Oxford PlasmaLab 100 (Oxford 100) etcher

Recipe: Oxygen plasma clean on blank Si wafer, time = 10 minutes

CHF<sub>3</sub>O<sub>2</sub> oxide etch season on blank Si wafer, time = 3 minutes

CHF<sub>3</sub>O<sub>2</sub> oxide etch on sample, time = 52 seconds

## **15. Metrology**

Equipment: P-10 profilometer and FilMetrics F40/F50-EXR

Recipe: Measure step height on P-10 profilometer

Measure oxide hard mask - silicon - buried oxide stack on filmetrics

Use measurements to determine if oxide hard mask is completely etched

## **16. Remove e-beam resist**

Equipment: Oxford PlasmaLab 80+ (Oxford 81/82) etcher

Recipe: Oxygen plasma clean on sample, time = 1min 45s

## **17. Step height measurement**

Equipment: P-10 profilometer

Recipe: Measure step height on P-10 profilometer after resist removal to obtain depth of over etch into silicon

## **18. Silicon device layer etch**

Equipment: Plasmatherm 770 (PT 770) etcher

Recipe: Season on dummy silicon wafer using process flow ssridar.prc, time = 4 minutes  
Etch sample using ssridar.prc, time = 50s

## **19. Metrology**

Equipment: P-10 profilometer and FilMetrics F40/F50-EXR

Recipe: Measure step height on P-10 profilometer

Measure oxide hard mask - silicon - buried oxide stack on filmetrics

Use measurements to determine if silicon device layer is completely etched

## **20. Oxide hard mask removal**

Equipment: Oxford PlasmaLab 80+ (Oxford 82) etcher

Recipe: Oxygen plasma clean on empty chamber, time = 10 minutes

CHF<sub>3</sub>O<sub>2</sub> oxide etch season on empty chamber, time = 3 minutes

CHF<sub>3</sub>O<sub>2</sub> oxide etch on sample, time = 37s

WITHOUT VENTING, oxygen plasma clean on sample, time = 1min

## **21. Surface clean/preparation**

Equipment: Acid chemical hood

Recipe: 2 minute dip in Nanostrip

Rinse in DI H<sub>2</sub>O

## **22. Photo resist spin**

Equipment: Photo resist spinners

Recipe: Spin P20 primer with parameters:

(wait 10s before spinning)

Speed = 3000rpm, ramp = 1000 rpm/s, time = 30s

Spin SPR 220-3.0 photo resist with parameters:

Speed = 3000rpm, ramp = 1000 rpm/s, time = 30s

Hard bake at 115°C for 90s

## **23. Expose - ion implant mask**

Equipment: Flexible 200mm Mask Aligner (ABM contact aligner)

Recipe: Exposure time = 8s

Post exposure bake at 115°C for 90s

## **24. Develop photo resist**

Equipment: General chemistry hoods

Recipe: 80s in 726MIF developer

## **25. Descum after developing resist**

Equipment: Oxford PlasmaLab 80+ (Oxford 81/82) etcher

Recipe: Oxygen plasma clean on empty chamber, time = 10 minutes

Oxygen plasma clean on sample, time = 1min 30s

## 26. Ion implantation

Equipment: Eaton Ion Implanter

Recipe: Boron ion implantation at 30keV, Dose =  $2 \times 10^{15}$

Keep current low to prevent photo resist burning

## 27. Remove photo resist

Equipment: General Chemistry hood

Recipe: 20 minute acetone dip with ultrasonic agitation

5 minute isopropyl alcohol dip with ultrasonic agitation

Rinse with DI H<sub>2</sub>O

## 28. MOS clean

Equipment: MOS clean wet bench

Recipe: 10 minutes dip in 1:1:6 NH<sub>4</sub>OH:H<sub>2</sub>O<sub>2</sub>:H<sub>2</sub>O at 70°C

10 minutes dip in 1:1:6 HCl:H<sub>2</sub>O<sub>2</sub>:H<sub>2</sub>O at 70°C

Rinse in DI H<sub>2</sub>O

## 29. Furnace anneal

Equipment: MRL Industries furnace (MOS clean anneal furnace - B1)

Recipe: Load sample at 800°C

Ramp to 900°C, time = 20min

Nitrogen anneal at 900°C, time = 5min

Cool to 650°C, time = 20min

Unload at 7% unload rate at 650°C

## 30. Surface clean/preparation

Equipment: Acid chemical hood

Recipe: 2 minute dip in Nanostrip

Rinse in DI H<sub>2</sub>O

Dehydration bake at 200°C for 5 minutes

### **31. LOR resist spin**

Equipment: Photo resist spinners

Recipe: Spin LOR 5A photo resist with parameters:

Speed = 500 rpm, ramp = 1000 rpm/s, time = 10s

Speed = 3000 rpm, ramp = 500 rpm/s, time = 50s

Hard bake at 170°C for 5 minutes

### **32. SPR 220-3.0 resist spin**

Equipment : Photo resist spinners

Recipe: Spin SPR 220-3.0 photo resist with parameters:

Speed = 3000 rpm, ramp = 1000 rpm/s, time = 30s

Hard bake at 115°C for 90s

### **33. Expose - metal mask**

Equipment: Flexible 200mm Mask Aligner (ABM contact aligner)

Recipe: Exposure time = 12s

Post exposure bake at 115°C for 90s

### **34. Develop photo resist**

Equipment: General chemistry hoods

Recipe: 2min 30s in 726MIF developer

### **35. Descum after developing resist**

Equipment: Oxford PlasmaLab 80+ (Oxford 81/82) etcher

Recipe: Oxygen plasma clean on empty chamber, time = 10 minutes

Oxygen plasma clean on sample, time = 30s

### **36. Pad surface clean**

Equipment: Acid chemical hood

Recipe: 30s dip in Buffered Oxide Etchant (BOE) 6:1

Rinse in DI H<sub>2</sub>O

This step is performed right before placing the chip in the evaporator to ensure there is no oxide on the pad area.

### **37. Metal evaporation**

Equipment: CVC SC4500 evaporation system (odd-hour evaporator)

Recipe: Evaporate 25nm nickel, deposition rate = 0.09 nm/s

Evaporate 25nm titanium, deposition rate = 0.19 nm/s

Evaporate 50nm platinum, deposition rate = 0.02 nm/s

Do not expose the sample to air between deposition materials

### **38. Lift-off**

Equipment: General chemistry hoods

Recipe: 20 min 1165 dip with ultrasonic agitation

Rinse with DI H<sub>2</sub>O

### **39. Furnace anneal**

Equipment: MRL Industries furnace (MOS metal anneal furnace - C2)

Recipe: Load sample at 400°C

5% H<sub>2</sub>/N<sub>2</sub> anneal at 400°C, time = 30min

Unload at 10% unload rate at 400°C

#### **40. Surface clean/preparation**

Equipment: Acid chemical hood

Recipe: 2 minute dip in Nanostrip

Rinse in DI H<sub>2</sub>O

#### **41. Vapor prime**

Equipment: YES LP-III (HMDS Vapor Prime oven)

Recipe: Standard HMDS vapor prime recipe

#### **42. Photo resist spin**

Equipment: Photo resist spinners

Recipe: Spin SPR 220-3.0 photo resist with parameters:

Speed = 3000rpm, ramp = 1000 rpm/s, time = 30s

Hard bake at 115°C for 90s

#### **43. Expose - release mask**

Equipment: Flexible 200mm Mask Aligner (ABM contact aligner)

Recipe: Exposure time = 8s

Post exposure bake at 115°C for 90s

#### **44. Develop photo resist**

Equipment: General chemistry hoods

Recipe: 80s in 726MIF developer

#### **45. Descum after developing resist**

Equipment: Oxford PlasmaLab 80+ (Oxford 81/82) etcher

Recipe: Oxygen plasma clean on empty chamber, time = 10 minutes

Oxygen plasma clean on sample, time = 1min 30s

#### **46. Hard bake**

Equipment: Photo resist/E-beam resist hotplates

Recipe: Hard bake at 145°C for 20min

#### **47. Timed release etch**

Equipment: Acid chemical hood

Recipe: 39min dip in BOE 6:1 for 6 $\mu$ m wide ring

23min 30s dip in BOE 6:1 for 3.7 $\mu$ m wide ring

5min rinse in DI H<sub>2</sub>O

a second 5min rinse in DI H<sub>2</sub>O

#### **48. Resist strip and CPD preparation**

Equipment: Base/solvent chemical hood

Recipe: 10min dip in acetone for resist removal

5min rinse in 1:1 isopropyl alcohol:DI H<sub>2</sub>O

5min rinse in isopropyl alcohol

#### **49. Critical point drying**

Equipment: Leica CPD300 critical point dryer (Leica CPD)

Recipe: Transfer sample to critical point dryer without exposing to air

Run recipe with the following parameters:

40% spinner speed

med. CO<sub>2</sub> input speed

83% filler capacity

120s delay time

4 exchange speed

20 exchange cycles

med. heating speed

slow 70% gas out speed

### **A.2.2 List of Process Steps for Short Run**

This silicon opto-mechanical resonator process flow is shorter by excluding the series of steps involved in ion implantation and metal evaporation. For low frequency resonators (kHz-MHz), this process flow can produce devices with good performance while significantly reducing the total fabrication time.

#### **1. Measure SOI stack**

Equipment: FilMetrics F40/F50-EXR

Measure the initial stack height to establish the starting Si device layer and buried oxide thickness.

#### **2. MOS clean**

Equipment: MOS clean wet bench

Recipe: 10 minutes dip in 1:1:6 NH<sub>4</sub>OH:H<sub>2</sub>O<sub>2</sub>:H<sub>2</sub>O at 70°C

10 minutes dip in 1:1:6 HCl:H<sub>2</sub>O<sub>2</sub>:H<sub>2</sub>O at 70°C

Rinse in De-Ionized (DI) H<sub>2</sub>O

### **3. Grow thermal oxide : hard mask creation**

Equipment: MRL Industries furnace (Wet/Dry Oxide furnace - B2)

Recipe: 23 minutes at 900°C using wet HCl oxidation to obtain 50nm oxide hard mask.

### **4. Measure oxidized stack**

Equipment: FilMetrics F40/F50-EXR

Measure the stack height after thermal oxidation to establish the oxide hard mask layer, Si device layer, and buried oxide layer thicknesses.

### **5. Photo resist spin**

Equipment: Photo resist spinners

Recipe: Spin P20 primer with parameters:

(wait 10s before spinning)

Speed = 3000rpm, ramp = 1000 rpm/s, time = 30s

Spin SPR 220-3.0 photo resist with parameters:

Speed = 3000rpm, ramp = 1000 rpm/s, time = 30s

Hard bake at 115°C for 90s

### **6. Dice wafer**

Equipment: K&S 7100 Dicing Saw

Dice the 6 inch wafer into 2cm x 2cm square pieces.

### **7. Resist removal**

Equipment: General Chemistry hood

Recipe: 10 min acetone dip  
5 min isopropyl alcohol dip  
Rinse with DI H<sub>2</sub>O

## 8. Surface clean/preparation

Equipment: Acid chemical hood

Recipe: 2 minute dip in Nanostrip  
Rinse in DI H<sub>2</sub>O

## 9. E-beam resist spin

Equipment: E-beam resist spinner

Recipe: Spin Ma-N 2403 e-beam resist with parameters:

Speed = 5000rpm, ramp = 2000 rpm/s, time = 30s

Hard bake at 90°C for 1 minute

## 10. E-beam lithography

Equipment: JEOL JBX9500FS (JEOL 9500) e-beam lithography system

Recipe: Expose at 2nA with doses:

1000 $\mu$ C/cm<sup>2</sup> for waveguides

850 $\mu$ C/cm<sup>2</sup> for gratings

500 $\mu$ C/cm<sup>2</sup> for the resonators

550 $\mu$ C/cm<sup>2</sup> for the tunable waveguide supports

400 $\mu$ C/cm<sup>2</sup> for the electrical routing and probe pads

## 11. Develop e-beam resist

Equipment: Electron beam resist hood

Recipe: 75s in 726MIF developer

## **12. Resist height measurement**

Equipment: P-10 profilometer

Measure step height of the e-beam resist across alignment marks.

## **13. Descum after developing resist**

Equipment: Oxford PlasmaLab 80+ (Oxford 81/82) etcher

Recipe: Oxygen plasma clean on empty chamber, time = 10 minutes

Oxygen plasma clean recipe on sample, time = 9s

## **14. Oxide hard mask etch**

Equipment: Oxford PlasmaLab 100 (Oxford 100) etcher

Recipe: Oxygen plasma clean on blank Si wafer, time = 10 minutes

CHF<sub>3</sub>O<sub>2</sub> oxide etch season on blank Si wafer, time = 3 minutes

CHF<sub>3</sub>O<sub>2</sub> oxide etch on sample, time = 52 seconds

## **15. Metrology**

Equipment: P-10 profilometer and FilMetrics F40/F50-EXR

Recipe: Measure step height on P-10 profilometer

Measure oxide hard mask - silicon - buried oxide stack on filmetrics

Use measurements to determine if oxide hard mask is completely etched

## **16. Remove e-beam resist**

Equipment: Oxford PlasmaLab 80+ (Oxford 81/82) etcher

Recipe: Oxygen plasma clean on sample, time = 1min 45s

## **17. Step height measurement**

Equipment: P-10 profilometer

Recipe: Measure step height on P-10 profilometer after resist removal to obtain depth of over etch into silicon

## **18. Silicon device layer etch**

Equipment: Plasmatherm 770 (PT 770) etcher

Recipe: Season on dummy silicon wafer using process flow ssridar.prc, time = 4 minutes  
Etch sample using ssridar.prc, time = 50s

## **19. Metrology**

Equipment: P-10 profilometer and FilMetrics F40/F50-EXR

Recipe: Measure step height on P-10 profilometer

Measure oxide hard mask - silicon - buried oxide stack on filmetrics

Use measurements to determine if silicon device layer is completely etched

## **20. Oxide hard mask removal**

Equipment: Oxford PlasmaLab 80+ (Oxford 82) etcher

Recipe: Oxygen plasma clean on empty chamber, time = 10 minutes

CHF<sub>3</sub>O<sub>2</sub> oxide etch season on empty chamber, time = 3 minutes

CHF<sub>3</sub>O<sub>2</sub> oxide etch on sample, time = 37s

WITHOUT VENTING, oxygen plasma clean on sample, time = 1min

## **21. Surface clean/preparation**

Equipment: Acid chemical hood

Recipe: 2 minute dip in Nanostrip

Rinse in DI H<sub>2</sub>O

## **22. Photo resist spin**

Equipment: Photo resist spinners

Recipe: Spin P20 primer with parameters:

(wait 10s before spinning)

Speed = 3000rpm, ramp = 1000 rpm/s, time = 30s

Spin SPR 220-3.0 photo resist with parameters:

Speed = 3000rpm, ramp = 1000 rpm/s, time = 30s

Hard bake at 115°C for 90s

## **23. Expose - metal mask**

Equipment: Flexible 200mm Mask Aligner (ABM contact aligner)

Recipe: Exposure time = 8s

Post exposure bake at 115°C for 90s

## **24. Develop photo resist**

Equipment: General chemistry hoods

Recipe: 80s in 726MIF developer

## **25. Descum after developing resist**

Equipment: Oxford PlasmaLab 80+ (Oxford 81/82) etcher

Recipe: Oxygen plasma clean on empty chamber, time = 10 minutes

Oxygen plasma clean on sample, time = 1min 30s

**26. Pad surface clean**

Equipment: Acid chemical hood

Recipe: 30s dip in Buffered Oxide Etchant (BOE) 6:1

Rinse in DI H<sub>2</sub>O

This step is performed to ensure there is no oxide on the pad area.

**27. Surface clean/preparation**

Equipment: Acid chemical hood

Recipe: 2 minute dip in Nanostrip

Rinse in DI H<sub>2</sub>O

**28. Vapor prime**

Equipment: YES LP-III (HMDS Vapor Prime oven)

Recipe: Standard HMDS vapor prime recipe

**29. Photo resist spin**

Equipment: Photo resist spinners

Recipe: Spin SPR 220-3.0 photo resist with parameters:

Speed = 3000rpm, ramp = 1000 rpm/s, time = 30s

Hard bake at 115°C for 90s

**30. Expose - release mask**

Equipment: Flexible 200mm Mask Aligner (ABM contact aligner)

Recipe: Exposure time = 8s

Post exposure bake at 115°C for 90s

### **31. Develop photo resist**

Equipment: General chemistry hoods

Recipe: 80s in 726MIF developer

### **32. Descum after developing resist**

Equipment: Oxford PlasmaLab 80+ (Oxford 81/82) etcher

Recipe: Oxygen plasma clean on empty chamber, time = 10 minutes

Oxygen plasma clean on sample, time = 1min 30s

### **33. Hard bake**

Equipment: Photo resist/E-beam resist hotplates

Recipe: Hard bake at 145°C for 20min

### **34. Timed release etch**

Equipment: Acid chemical hood

Recipe: 39min dip in BOE 6:1 for 6 $\mu$ m wide ring

23min 30s dip in BOE 6:1 for 3.7 $\mu$ m wide ring

5min rinse in DI H<sub>2</sub>O

a second 5min rinse in DI H<sub>2</sub>O

### **35. Resist strip and CPD preparation**

Equipment: Base/solvent chemical hood

Recipe: 10min dip in acetone for resist removal

5min rinse in 1:1 isopropyl alcohol:DI H<sub>2</sub>O

5min rinse in isopropyl alcohol

### 36. Critical point drying

Equipment: Leica CPD300 critical point dryer (Leica CPD)

Recipe: Transfer sample to critical point dryer without exposing to air

Run recipe with the following parameters:

40% spinner speed

med. CO<sub>2</sub> input speed

83% filler capacity

120s delay time

4 exchange speed

20 exchange cycles

med. heating speed

slow 70% gas out speed

## BIBLIOGRAPHY

- [1] J. T. M. van Beek and R. Puers, “A review of mems oscillators for frequency reference and timing applications,” *Journal of Micromechanics and Microengineering*, vol. 22, no. 1, p. 013001, 2012. [Online]. Available: <http://stacks.iop.org/0960-1317/22/i=1/a=013001>
- [2] C.-C. Nguyen, “Mems technology for timing and frequency control,” *Ultrasonics, Ferroelectrics and Frequency Control, IEEE Transactions on*, vol. 54, no. 2, pp. 251–270, 2007.
- [3] C. S. Lam, “A review of the recent development of mems and crystal oscillators and their impacts on the frequency control products industry,” in *Ultrasonics Symposium, 2008. IUS 2008. IEEE*, 2008, pp. 694–704.
- [4] S. Tabatabaei and A. Partridge, “Silicon mems oscillators for high-speed digital systems,” *Micro, IEEE*, vol. 30, no. 2, pp. 80–89, 2010.
- [5] C. Enz, J. Baborowski, J. Chabloz, M. Kucera, C. Muller, D. Ruffieux, and N. Scolari, “Ultra low-power mems-based radio for wireless sensor networks,” in *Circuit Theory and Design, 2007. ECCTD 2007. 18th European Conference on*, 2007, pp. 320–331.
- [6] S. Bhave, “Hybrid mems resonators and oscillators,” in *Frequency Control and the European Frequency and Time Forum (FCS), 2011 Joint Conference of the IEEE International*, 2011, pp. 1–6.
- [7] D. Weinstein and S. A. Bhave, “The resonant body transistor,” *Nano Letters*, vol. 10, no. 4, pp. 1234–1237, 2010, pMID: 20180594. [Online]. Available: <http://pubs.acs.org/doi/abs/10.1021/nl9037517>
- [8] W. Wang, L. Popa, R. Marathe, and D. Weinstein, “An unreleased mm-wave resonant body transistor,” in *Micro Electro Mechanical Systems (MEMS), 2011 IEEE 24th International Conference on*, 2011, pp. 1341–1344.
- [9] S. Tallur, S. Sridaran, and S. Bhave, “A silicon nitride optomechanical oscillator with zero flicker noise,” in *2012 IEEE 25th International Conference on Micro Electro Mechanical Systems (MEMS)*, Jan. 2012, pp. 19–22.
- [10] S. Tallur and S. Bhave, “Monolithic 2ghz electrostatically actuated MEMS oscillator with opto-mechanical frequency multiplier,” in *2013 Transducers Eurosensors XXVII: The 17th International Conference on Solid-State Sensors*,

*Actuators and Microsystems (TRANSDUCERS EUROSENSORS XXVII)*, Jun. 2013, pp. 1472–1475.

- [11] C. Rembe and R. Muller, “Measurement system for full three-dimensional motion characterization of mems,” *Microelectromechanical Systems, Journal of*, vol. 11, no. 5, pp. 479–488, 2002.
- [12] J. V. Knuuttila, P. T. Tikka, and M. M. Salomaa, “Scanning michelson interferometer for imaging surface acoustic wave fields,” *Opt. Lett.*, vol. 25, no. 9, pp. 613–615, May 2000. [Online]. Available: <http://ol.osa.org/abstract.cfm?URI=ol-25-9-613>
- [13] H. Chandralalim, S. Bhave, R. Polcawich, J. Pulskamp, B. Pourat, S. Boedecker, and C. Rembe, “Heterodyne laser-doppler interferometric characterization of contour-mode resonators above 1 ghz,” in *Ultrasonics Symposium (IUS), 2009 IEEE International*, 2009, pp. 1044–1049.
- [14] V. B. Braginsky, *Measurement of Weak Forces in Physics Experiments*. University of Chicago Press, Chicago, 1977.
- [15] T. J. Kippenberg and K. J. Vahala, “Cavity opto-mechanics,” *Opt. Express*, vol. 15, no. 25, pp. 17 172–17 205, Dec 2007. [Online]. Available: <http://www.opticsexpress.org/abstract.cfm?URI=oe-15-25-17172>
- [16] T. Rocheleau, A. Grine, K. Grutter, R. Schneider, N. Quack, M. Wu, and C.-C. Nguyen, “Enhancement of mechanical q for low phase noise optomechanical oscillators,” in *2013 IEEE 26th International Conference on Micro Electro Mechanical Systems (MEMS)*, Jan. 2013, pp. 118–121.
- [17] S. Sridaran and S. Bhave, “Opto-acoustic oscillator using silicon MEMS optical modulator,” in *Solid-State Sensors, Actuators and Microsystems Conference (TRANSDUCERS), 2011 16th International*, Jun. 2011, pp. 2920–2923.
- [18] T. J. Kippenberg and K. J. Vahala, “Cavity optomechanics: Back-action at the mesoscale,” *Science*, vol. 321, no. 5893, pp. 1172–1176, Aug. 2008. [Online]. Available: <http://www.sciencemag.org/content/321/5893/1172>
- [19] M. Poot, K. Y. Fong, M. Bagheri, W. H. P. Pernice, and H. X. Tang, “Backaction limits on self-sustained optomechanical oscillations,” *Physical Review A*, vol. 86, no. 5, p. 053826, Nov. 2012. [Online]. Available: <http://link.aps.org/doi/10.1103/PhysRevA.86.053826>

- [20] A. Schliesser, R. Riviere, G. Anetsberger, O. Arcizet, and T. J. Kippenberg, “Resolved-sideband cooling of a micromechanical oscillator,” *Nature Physics*, vol. 4, no. 5, pp. 415–419, May 2008. [Online]. Available: <http://www.nature.com/nphys/journal/v4/n5/full/nphys939.html>
- [21] G. I. Harris, U. L. Andersen, J. Knittel, and W. P. Bowen, “Feedback-enhanced sensitivity in optomechanics: Surpassing the parametric instability barrier,” *Physical Review A*, vol. 85, no. 6, p. 061802, Jun. 2012. [Online]. Available: <http://link.aps.org/doi/10.1103/PhysRevA.85.061802>
- [22] H. Rokhsari, M. Hossein-Zadeh, A. Hajimiri, and K. Vahala, “Brownian noise in radiation-pressure-driven micromechanical oscillators,” *Applied Physics Letters*, vol. 89, no. 26, p. 261109, Dec. 2006. [Online]. Available: <http://scitation.aip.org/content/aip/journal/apl/89/26/10.1063/1.2424276>
- [23] A. Schliesser, G. Anetsberger, R. Riviere, O. Arcizet, and T. J. Kippenberg, “High-sensitivity monitoring of micromechanical vibration using optical whispering gallery mode resonators,” *New Journal of Physics*, vol. 10, no. 9, p. 095015, Sep. 2008. [Online]. Available: <http://iopscience.iop.org/1367-2630/10/9/095015>
- [24] S. Sridaran and S. A. Bhave, “Electrostatic actuation of silicon optomechanical resonators,” *Optics Express*, vol. 19, no. 10, p. 9020, May 2011. [Online]. Available: <http://www.opticsinfobase.org/oe/abstract.cfm?uri=oe-19-10-9020>
- [25] M. Li, W. Pernice, and H. Tang, “Reactive cavity optical force on microdisk-coupled nanomechanical beam waveguides,” *Physical Review Letters*, vol. 103, no. 22, p. 223901, Nov. 2009. [Online]. Available: <http://link.aps.org/doi/10.1103/PhysRevLett.103.223901>
- [26] J. Rosenberg, Q. Lin, and O. Painter, “Static and dynamic wavelength routing via the gradient optical force,” *Nature Photonics*, vol. 3, no. 8, pp. 478–483, Aug. 2009. [Online]. Available: <http://www.nature.com/nphoton/journal/v3/n8/full/nphoton.2009.137.html>
- [27] Y. Xie, S.-S. Li, Y.-W. Lin, Z. Ren, and C.-C. Nguyen, “UHF micromechanical extensional wine-glass mode ring resonators,” in *Electron Devices Meeting, 2003. IEDM '03 Technical Digest. IEEE International*, Dec. 2003, pp. 39.2.1–39.2.4.
- [28] M. Hopcroft, W. Nix, and T. Kenny, “What is the young’s modulus of silicon?”

*Journal of Microelectromechanical Systems*, vol. 19, no. 2, pp. 229–238, Apr. 2010.

- [29] X. Wei and A. A. Seshia, “Analytical formulation of modal frequency split in the elliptical mode of SCS micromechanical disk resonators,” *Journal of Micromechanics and Microengineering*, vol. 24, no. 2, p. 025011, Feb. 2014. [Online]. Available: <http://iopscience.iop.org/0960-1317/24/2/025011>
- [30] M. Abdelmoneum, M. Demirci, and C.-C. Nguyen, “Stemless wine-glass-mode disk micromechanical resonators,” in *IEEE The Sixteenth Annual International Conference on Micro Electro Mechanical Systems, 2003. MEMS-03 Kyoto*, Jan. 2003, pp. 698–701.
- [31] F. Ayazi and K. Najafi, “High aspect-ratio combined poly and single-crystal silicon (HARPSS) MEMS technology,” *Journal of Microelectromechanical Systems*, vol. 9, no. 3, pp. 288–294, Sep. 2000.
- [32] M. Soltani, “Novel integrated silicon nanophotonic structures using ultra-high q resonators,” Aug. 2009, ph.D. [Online]. Available: <https://smartech.gatech.edu/handle/1853/31647>
- [33] Y.-W. Lin, S.-S. Li, Z. Ren, and C.-C. Nguyen, “Low phase noise array-composite micromechanical wine-glass disk oscillator,” in *Electron Devices Meeting, 2005. IEDM Technical Digest. IEEE International*, Dec. 2005, pp. 4 pp.–281.
- [34] E. Shah Hosseini, “High quality integrated silicon nitride nanophotonic structures for visible light applications,” May 2011, ph.D. [Online]. Available: <http://smartech.gatech.edu/handle/1853/41052>
- [35] B. Dong, J. Huang, H. Cai, P. Kropelnicki, A. Randles, Y. Gu, and A. Liu, “Nano-opto-electro-mechanical (NOEM) oscillator with controllable non-linear dynamics,” in *2014 IEEE 27th International Conference on Micro Electro Mechanical Systems (MEMS)*, Jan. 2014, pp. 1261–1264.
- [36] S. Pamidighantam, R. Puers, K. Baert, and H. A. C. Tilmans, “Pull-in voltage analysis of electrostatically actuated beam structures with fixedfixed and fixedfree end conditions,” *Journal of Micromechanics and Microengineering*, vol. 12, no. 4, p. 458, Jul. 2002. [Online]. Available: <http://iopscience.iop.org/0960-1317/12/4/319>
- [37] H. Johari, “Micromachined capacitive silicon bulk acous-

tic wave gyroscopes,” Nov. 2008, ph.D. [Online]. Available: <https://smartech.gatech.edu/handle/1853/31656>

- [38] S. Tallur, “Leveraging opto-mechanics to design high performance rf oscillators,” Jan. 2014, ph.D. [Online]. Available: <http://ecommons.library.cornell.edu/handle/1813/36167>